

Thesis

Ekaterina Avdeeva

University of Nebraska-Lincoln, USA

January 10, 2017

Abstract

This paper reviews

Contents

8	1	Introduction	2
9	1.1	Fundamental Particles and Interactions	3
10	1.2	Electroweak Interactions	5
11	1.3	Strong Interactions	8
12	1.4	Physics of Proton-Proton Collisions	9
13	1.5	Open Questions of the Standard Model	11
14	2	$W\gamma$ Production Theory and Former Experimental Results	12
15	2.1	Electroweak Theory of the Standard Model	13
16	2.2	Cross Section and Luminosity	18
17	2.3	Standard Model $W\gamma$ Production	20
18	2.4	Anomalous $W\gamma$ Production	23
19	3	Experimental Setup	28
20	3.1	Large Hadron Collider	29
21	3.2	Compact Muon Solenoid	33
22	3.2.1	Introduction	33
23	3.2.2	Magnet	34
24	3.2.3	Tracking System	34
25	3.2.4	Electromagnetic Calorimeter	35
26	3.2.5	Hadron Calorimeter	36
27	3.2.6	Muon System	36
28	3.2.7	Triggering and Data Aquisition	37
29	3.2.8	Particle Flow Algorithm of Event Reconstruction	37
30	4	CMS Tracker Alignment	39
31	4.1	Algorithm	40
32	4.2	Selected Results	45
33	5	$W\gamma$ Cross Section Measurement	46

34 1 Introduction

35 Elementary particle physics describes fundamental particles and their interactions. Fundamental
36 particles are the smallest constituents of our Universe. When examined at smaller scales, the
37 substances around us consist of molecules, molecules consist of atoms. In an atom there is a
38 nucleus made of neutrons and protons and some number of electrons occupying orbits around
39 the nucleus. Protons and neutrons have a structure while an electron is not known to have any
40 internal structure, therefore, an electron is an example of a particle which is considered to be
41 fundamental.

42

43 Interactions of elementary particles are described by quantum field theories which incorporate
44 principles of the quantum mechanics and the special theory of relativity. The set of such theories,
45 including quantum electrodynamics (QED), quantum chromodynamics (QCD) and the theory
46 of weak interactions is called the Standard Model (SM). Current observations have proved the
47 SM to be an accurate description of elementary particle interactions.

48

49 However, there are several experimental observations that are not described by the SM such
50 as effects of gravity, dark matter, dark energy, matter/antimatter asymmetry and others. There-
51 fore, the SM is not the complete theory of particle interactions. There are several SM extensions
52 offered by theorists as well as radically new theories waiting for experimental confirmation or
53 exclusion.

54

55 Some SM extensions and new theories predict the existence of heavy particles with masses
56 lying beyond experimentally reachable energies. The search of these particles is a priority in
57 particle physics. One source of highly energetic elementary particles is cosmic rays. The most
58 energetic particles ever observed came from this source. However, cosmic rays are totally uncon-
59 trollable and such highly energetic particles are rare. If we want to produce a large number of
60 particles in a given energy range, we need to use a particle accelerator. A large amount of data
61 allows experimentalists to perform a statistical analysis and increase the probability of finding a
62 new particle if it exists.

63

64 Symmetric colliding beams is the most effective way to produce as heavy particles as possible
65 given the energies of the colliding particles. Compared to experiments colliding a single beam at
66 a fixed target, in the case of a symmetric collision the total momentum of two colliding particles
67 is zero and, therefore, much larger fraction of energy can transfer to a mass of a new particle.
68 The Large Hadron Collider (LHC) is one such collider with the highest energy in the world. It
69 can produce the most massive particles to probe physics beyond the SM (BSM).

70

71 The Compact Muon Solenoid (CMS) is one of two general-purpose detectors at the LHC. It
72 is placed at one of four collision points. CMS has a broad physics program including searches for
73 the BSM physics as well as the precision measurements of the parameters of the SM itself. The
74 measurement of this dissertation is a SM measurement with CMS data collected in 2012 in pp
75 collisions of LHC with beam energies of 4 TeV. The result can be compared to the SM prediction.
76 Certain BSM theories predict a deviation of the result of this measurement from its SM value,
77 therefore, with this measurement, in addition to testing the SM, we also search for a new physics.

78

79 The rest of this chapter gives general introductory information about the SM while Ch. 2
80 concentrates on the theory of the SM and BSM $W\gamma$ production and also discusses previous
81 measurements of this process. Chapter 3 describes LHC and CMS in more details. Chapter 4
82 explains one specific detail of the CMS operation that is the spacial alignment of the tracking
83 detector of charged particles. Finally, Ch. 5 describes the details of the measurement of this
84 dissertation and reports the results.

85

86 1.1 Fundamental Particles and Interactions

87 The SM describes interactions of elementary particles. There are four fundamental interactions:
88 electromagnetic, strong, weak and gravitational. The gravity is not included into the SM but its
89 effect on particles is negligible compared to the other forces which makes it possible to develop a
90 theory of the particle physics and conduct experiments even without having the gravity included
91 into the model.

92 All fundamental elementary particles in the SM can be split into three categories by their
93 spins. There are fermions which possess spin $s=1/2$, there are gauge bosons which are vector
94 particles ($s=1$) and there is the Higgs boson which is a scalar particle ($s=0$).

95 The fermions are arranged into three generations, each generation consists of a quark with
96 charge $Q=+2/3$ (up, charm, and top quarks), a quark with $Q=-1/3$ (down, strange, and bottom
97 quarks), a charged lepton with $Q=-1$ (electron, muon, and tau-lepton) and a neutrino (electron,
98 muon, and tau neutrinos) which is electrically neutral. Each quark can carry any of three colors:
99 red, blue, or green. Additionally, each fermion has its antiparticle. Therefore, the total number
100 of fundamental fermions is $(6(\text{leptons}) + 6(\text{quarks}) \cdot 3(\text{colors})) \cdot 2(\text{to include antiparticles}) = 48$.

101 Corresponding particles in different generations have the same charges, spins and interaction
102 properties but masses of particles increase with a generation. These mass differences lead
103 to different decay properties because a particle A can decay to particles B and C only if their
104 masses relate as $m_A > m_B + m_C$. Thus, an electron is a stable particle, a muon decays as
105 $\mu^- \rightarrow e^- + \bar{\nu}_e + \nu_\mu$, a tau-lepton, as the heaviest charged lepton, has the largest number of decay
106 channels amongst the charged leptons: $\tau^- \rightarrow \mu^- + \bar{\nu}_\mu + \nu_\tau$, $\tau^- \rightarrow e^- + \bar{\nu}_e + \nu_\tau$, $\tau^- \rightarrow \nu_\tau + \text{quarks}$.

107 In addition to fermions, the SM includes gauge bosons which are interaction mediators. They
108 are called mediators because fermions interact with each other by exchanging them. For example,
109 two charged fermions can interact with each other by exchanging a photon. Such interaction is
110 called electromagnetic interaction and a photon is a mediator for the electromagnetic interaction.
111 Similarly, a gluon is a mediator for strong interactions, and W^\pm and Z^0 bosons are mediators
112 for weak interactions. W^\pm and Z^0 bosons are massive while a photon and a gluon are massless
113 particles.

114 The last SM particle is the Higgs boson. The Higgs boson is a scalar neutral particle which
115 is playing a critical role in the electroweak symmetry breaking. The Higgs mechanism explains
116 how W and Z bosons become massive particles.

117 All the particles are summarized in Fig. 1. These and only these fundamental particles and
118 their antiparticles have been discovered by now. However, there are many composite particles
119 which are called hadrons. Hadrons can consist of three quarks (baryons), quark and antiquark
120 (meson), or three antiquarks (antibaryons). Hadrons always possess an integer charge.

121 Most of the particles are short-lived and decay within microseconds. The only stable particles
122 are protons and antiprotons, electrons and positrons, neutrinos and antineutrinos, photons,
123 and, in some sense, gluons. However, if a particle cannot decay, it does not mean that it would
124 live forever. There are many different kinds of reactions in which particles can disappear. An-
125 tiprotons and positrons would immediately annihilate with protons and electrons, photons can
126 be absorbed by charged particles, electrons and protons can scatter to produce neutrons and
127 neutrinos and many other reactions are possible.

128 In this dissertation, the study of $pp \rightarrow W\gamma + X \rightarrow l\nu\gamma$ process where $l = e, \mu$ is presented. The
129 $W\gamma$ production with leptonic W decays proceeds through one of the following three processes:
130 the initial state radiation where a photon is emitted from one of the incoming partons, the final
131 state radiation where a photon is radiated off the charged lepton from the W boson decay, and,
132 finally, the triple gauge coupling (TGC) where a photon is emitted from the W boson. Many

141 BSM theories predict an enhancement of the TGC production over the SM value and, therefore,
 142 the experimental search for such an enhancement is a good test for such theories.

143

144 Therefore, the focus of this study is an interaction between a photon and a W boson however
 145 many other SM particles are relevant too. Thus, a charged lepton and a neutrino appear as the
 146 final state particles, a quark and an antiquark appear as initial state particles and all fundamen-
 147 tal particles except the Higgs boson participate in various background processes. Subsequent
 148 chapters describe these particle interactions in more details.

149

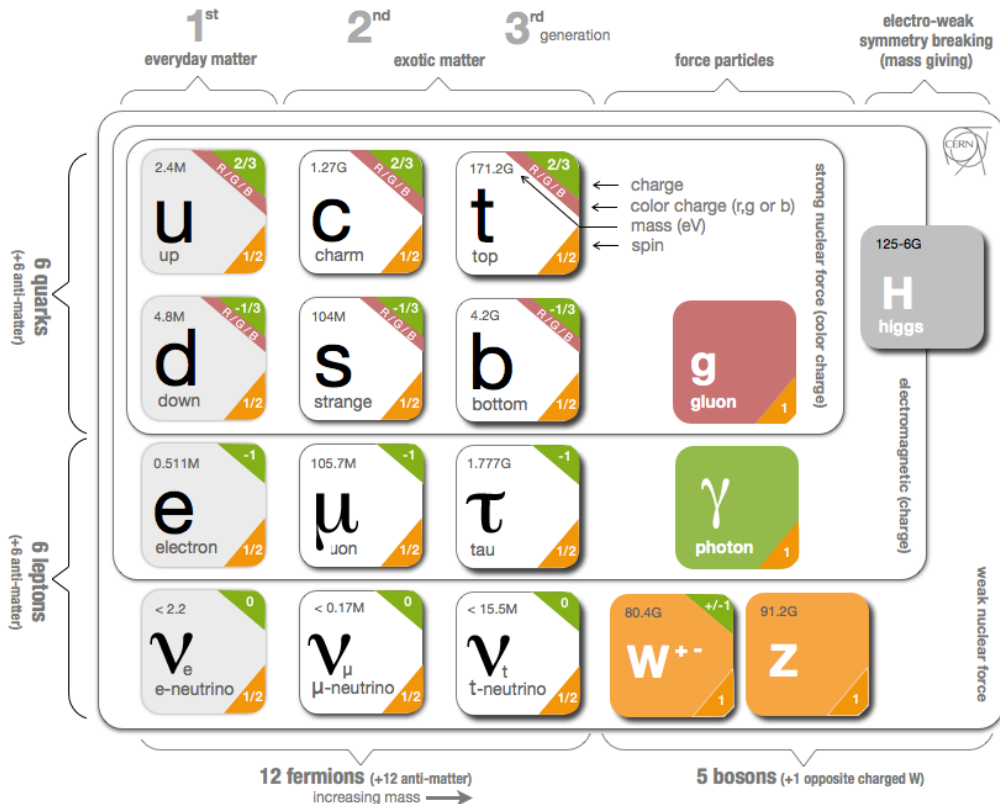


Figure 1: Standard Model Particles and Interactions. Source of the figure: [2].

150 **1.2 Electroweak Interactions**

151 All electrically charged particles participate in electromagnetic interactions. The theory of elec-
 152 tromagnetic interactions is called quantum electrodynamics (QED). All electromagnetic inter-
 153 actions are mediated by a photon, a spin-one electrically neutral massless particle, and can be
 154 reduced to one elementary process (Fig. 2, left). This process represents a charged fermion
 155 radiating or absorbing a photon. Such elementary process itself is forbidden by the energy con-
 156 servation law but this element is a base of an actual process. For example, the Bhabha scattering,
 157 $e^+e^- \rightarrow e^+e^-$, occurs through e^+e^- annihilation with further production of a new e^+e^- pair
 158 (Fig. 2, middle) or through exchange of a photon between the positron and the electron (Fig. 2,
 159 right). Both cases involve nothing except the electromagnetic elementary process (Fig. 2, left).
 160 Such graphical representations of the particle physics processes are called Feynman diagrams.

161

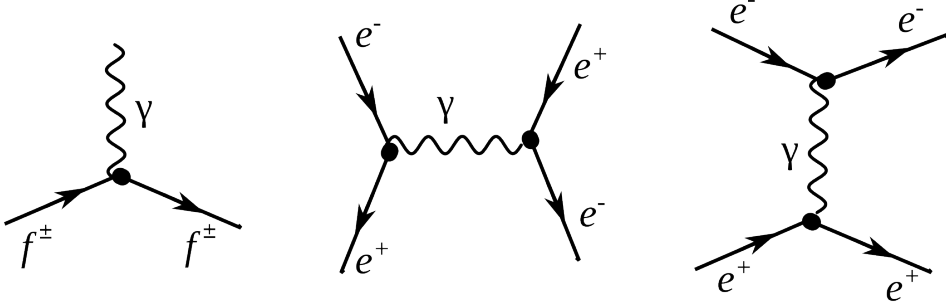


Figure 2: Electromagnetic interactions. Left: a photon radiation off a charged fermion, middle and right: Bhabha scattering.

162 As for the weak interactions, there are two kinds of them: neutral (mediated by a Z boson)
 163 and charged (mediated by a W^\pm boson). Elementary processes with W and Z bosons are shown
 164 in Fig. 3. Because the electric charge must be conserved at any vertex, a particle radiating or
 165 absorbing a W boson converts to a different particle. Thus, a charged lepton converts to a neu-
 166 trino (or vice versa) as shown in Fig. 3, top middle. Each lepton carries a lepton flavor number
 167 (Tab. 1). Lepton flavor is conserved in any interaction, thus an electron radiating a W boson
 168 always converts to an electron neutrino, a muon converts to a muon neutrino etc.

169

Table 1: Lepton Flavor Number

particles	L_e	L_μ	L_τ
e^-, ν_e	+1	0	0
$e^+, \bar{\nu}_e$	-1	0	0
μ^-, ν_μ	0	+1	0
$\mu^+, \bar{\nu}_\mu$	0	-1	0
τ^-, ν_τ	0	0	+1
$\tau^+, \bar{\nu}_\tau$	0	0	-1

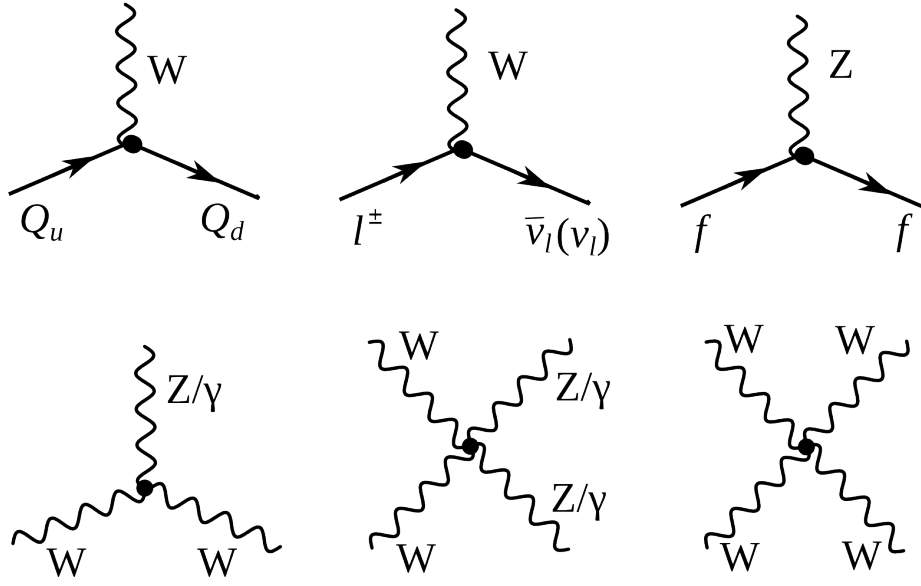


Figure 3: Weak elementary processes and gauge couplings. Top left: a quark with charge $Q=+2/3$ enters, emits a W boson, and a quark with charge $Q=-1/3$ escapes. Top middle: a charged lepton enters, emits a W boson, and a neutrino or antineutrino escapes conserving a lepton flavor number. Top right: a fermion enters, emits a Z boson and escapes. Bottom left: TGC couplings $WW\gamma$ and WWZ . Bottom middle: QGC couplings $WW\gamma\gamma$, $WWZ\gamma$ and $WWZZ$. Bottom right: QGC coupling $WWWW$.

From top left diagram in Fig. 3 we see that if a quark with $Q=+2/3$ enters, then a quark with $Q=-1/3$ escapes and, therefore, the flavor of the quark is changed. The charged weak interaction is the only interaction which changes a quark flavor. The probability of each of three quarks with $Q=-1/3$ to be born is determined by the Cabibbo-Kobayashi-Maskawa matrix which relates mass eigenstates d , c and b to weak eigenstates d' , c' and b' (Eq. 1). Absolute values of the matrix elements are all known (Eq. 2) and are the highest for the quark of the same generation as an initial state quark. In the particular case shown in the top left diagram in Fig. 3, u is the initial state quark and d has the highest probability to be produced after an interaction with a W boson but s and b can also be produced if there is enough energy.

179

$$\begin{pmatrix} d' \\ s' \\ b' \end{pmatrix} = \begin{pmatrix} V_{ud} & V_{us} & V_{ub} \\ V_{cd} & V_{cs} & V_{cb} \\ V_{td} & V_{ts} & V_{tb} \end{pmatrix} \begin{pmatrix} d \\ s \\ b \end{pmatrix} \quad (1)$$

$$\begin{pmatrix} |V_{ud}| & |V_{us}| & |V_{ub}| \\ |V_{cd}| & |V_{cs}| & |V_{cb}| \\ |V_{td}| & |V_{ts}| & |V_{tb}| \end{pmatrix} = \begin{pmatrix} 0.97 & 0.23 & 0.00 \\ 0.23 & 0.97 & 0.04 \\ 0.01 & 0.04 & 1.00 \end{pmatrix} \quad (2)$$

An elementary process of a neutral weak interaction is an emission a Z boson off a fermion line (right top diagram in Fig. 3). Diagrams with a Z boson are very similar to ones with a photon except a photon can only be radiated off a charged particle but a Z boson can also be radiated off a neutrino or antineutrino.

184

185 The bottom diagrams in Fig. 3 are gauge bosons coupling diagrams including self-coupling
 186 of a W boson, its interaction with a Z boson and its electromagnetic radiation of a photon.
 187 Charge-conserving TGC and quartic gauge couplings (QGC) containing two or four W bosons
 188 are all possible in the SM: WWZ , $WW\gamma$, $WWZZ$, $WWZ\gamma$, $WW\gamma\gamma$, and $WWWW$.
 189

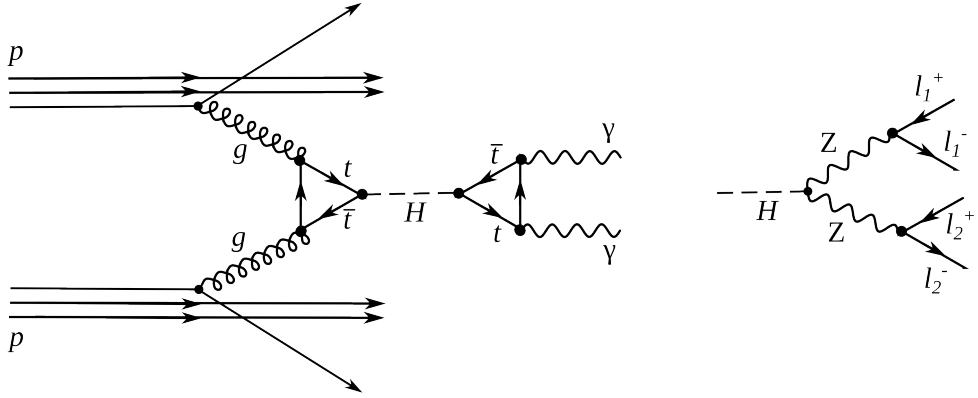
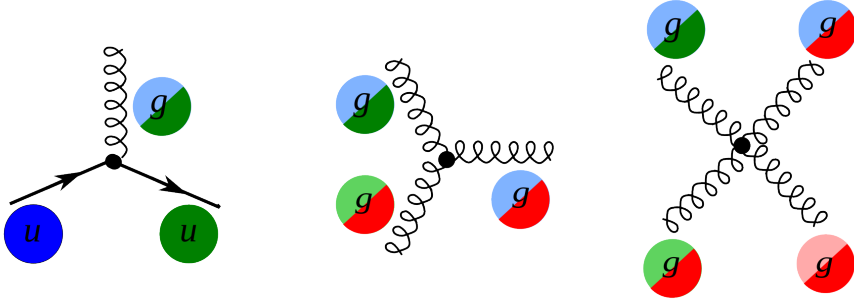


Figure 4: The Higgs boson production and decay. Left: $H \rightarrow \gamma\gamma$, right: $H \rightarrow ZZ \rightarrow 4l$.

190 Electromagnetic and weak interactions are unified by the electroweak Glashow-Weinberg-
 191 Salam (GWS) theory which is based on $SU(2) \times U(1)$ symmetry. $SU(2)$ is the symmetry of
 192 weak isospin which generates three bosons: W^1 , W^2 and W^3 . $U(1)$ is the symmetry of the weak
 193 hypercharge and generate one neutral boson B . W^1 and W^2 are mixed to create W^+ and W^-
 194 mediators while W^3 and B are mixed to create a Z boson and a photon. Therefore, the GWS
 195 theory considers electromagnetic and weak forces as different manifestations of the electroweak
 196 force. The electroweak theory is discussed in greater details in Ch. 2.

197 However, weak interactions are mediated by heavy bosons ($M_W = 80$ GeV, $M_Z = 91$ GeV)
 198 while electromagnetic interactions are mediated by a massless photon, thus, the electroweak
 199 symmetry is broken. To explain this phenomenon, the Higgs mechanism was introduced. The
 200 mechanism predicted an existence of an additional boson: the Higgs boson. The Higgs boson
 201 was a missing piece of the SM for many years and was finally discovered in 2012 at LHC by
 202 ATLAS and CMS collaborations through the processes shown in Fig. 4 [3], [4].
 203

204 The measurement in this dissertation is an electroweak measurement because the process
 205 involves a W boson. It includes an interaction of a W boson with leptons and quarks as well as
 206 the TGC $WW\gamma$. Thus, the measurement is a good test of the SM electroweak theory.
 207
 208

209 1.3 Strong Interactions


210 Figure 5: Elementary processes of strong interactions

211 The third fundamental force after the electromagnetic and weak ones is the strong force. The
 212 strong force is responsible for gluing protons and neutrons together in the nuclei as well as for
 213 forming protons and neutrons themselves. The strong interactions occur by exchanging gluons
 214 which are spin-one massless electrically neutral particles.

215 The elementary strong processes are shown in Fig. 5. There are three elementary processes:
 216 qqg , ggg and $gggg$, all are involving particles with color charges. Thus, gluons couple to quarks
 217 and self-couple. Color charges must be conserved at each elementary process of the strong inter-
 218 action. Each quark possesses one of three colors at a time, and there are eight types of gluons
 219 to cover all possible color exchanges.

220 The coupling constant of the strong interaction depends on a distance between interacting
 221 particles: it becomes larger as the distance becomes larger and smaller as the distance becomes
 222 smaller. As the distance approaches zero, the coupling constant approaches zero too, and, thus,
 223 in the asymptotic limit two quarks located at the same place do not interact. This property is
 224 called asymptotic freedom.

225 On the other hand, when the distance between quarks becomes larger, the coupling constant
 226 also becomes larger. This property confines quarks to always stay in the color neutral combi-
 227 nations (hadrons), it forbids the existence of free quarks. A combination becomes color neutral
 228 when there is the same amount of color and anticolor or if there is the same amount of each of
 229 the three colors. Thus, mesons are comprised of a quark and an antiquark with the opposite
 230 color charges, and baryons are comprised of three quarks: red, green and blue one. Examples of
 231 baryons include such well-known particles as a proton and a neutron.

232 The asymptotic freedom and the confinement are properties that are specific for strong inter-
 233 actions. The theory of strong interactions is called the quantum chromodynamics (QCD)
 234 which is a quantum field theory invariant under $SU(3)$ color transformations. When the cou-
 235 pling constant is much less than one $\alpha_s \ll 1$, the perturbative approach can be used to compute
 236 observables.

237 The $W\gamma$ process being measured in this dissertation is not intended to test QCD, but a good
 238 understanding of QCD is essential for performing this measurement because the QCD correc-
 239 tions to the Feynman diagrams of the process are large and have to be taken into account when
 240 producing simulation. In addition, QCD describes the dynamics of quarks and gluons within
 241 colliding protons and predicts probabilities of one or another quark-antiquark pair to interact.
 242 Physics of proton-proton collisions is discussed in the Ch. 1.4.

248 1.4 Physics of Proton-Proton Collisions

249 Consider a pp collision at LHC. The proton energies are so high that each proton behaves as a
 250 complex structure. A proton is a baryon, it consists of three quarks: uud . These three quarks
 251 are called valence quarks. They interact with each other by exchanging gluons which produce
 252 virtual $q\bar{q}$ pairs (Fig. 6). Such quarks are called sea quarks.

253 Any parton from one proton can interact with any parton from another proton. Probabilities
 254 $f_i(x, Q^2)$ of any particular constituent i to interact are described partially by QCD and parti-
 255 cally by experimental measurements and depend on the momentum transfer Q and the momen-
 256 tum fraction of a specific parton x . These probabilities are called parton distribution func-
 257 tions (PDFs).

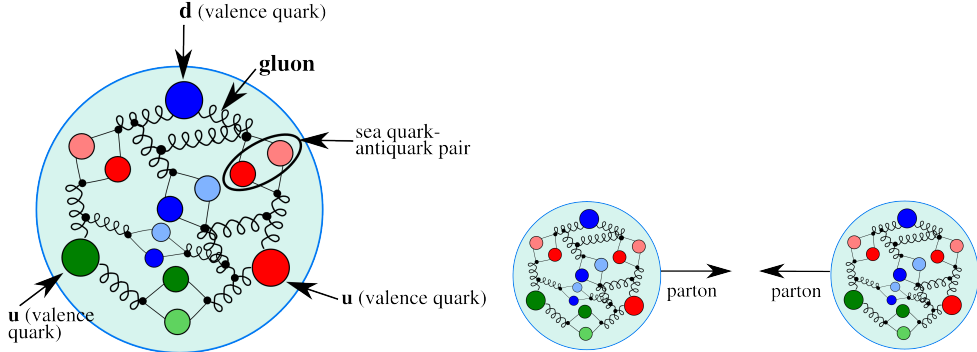


Figure 6: The proton structure (left) and the proton-proton collision (right).

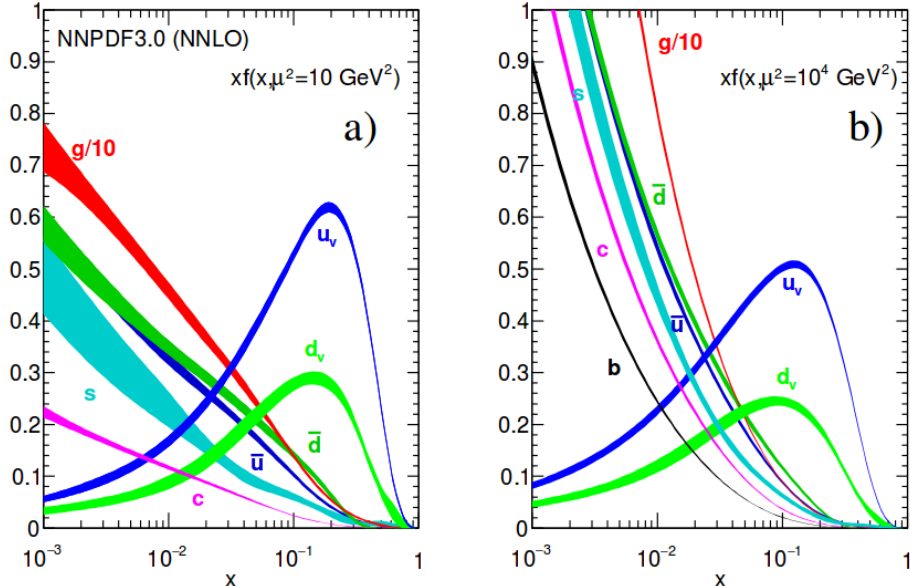


Figure 7: Parton distribution functions [5].

260 For large Q^2 and x gluon-gluon interactions have the largest probabilities to occur (Fig. 7).

261 However, gluons do not couple directly to a W boson, thus, in the $W\gamma$ measurement we are
262 mostly interested in quark-antiquark pairs which would have a total charge corresponding to the
263 charge of a W boson (± 1). Since we have u and d as valence quarks and we know that the
264 probability to couple to the same generation quark in charged weak interactions is the highest,
265 most of the W bosons are created by $u\bar{d}$ and $d\bar{u}$ pairs however other $q\bar{q}'$ combinations with the
266 total charges of ± 1 are also possible. As we look for events containing $W\gamma$ we also have other
267 events mimicking our process. Such background events can be produced by any pair of partons.

268

269 1.5 Open Questions of the Standard Model

270 While the SM is an accurate description of all particle physics experimental results, there are
271 certain phenomena which are not included into the SM. In this subsection we discuss some of
272 them.

273 The gravitational interactions do not fit into the SM. It is the open question whether the
274 quantum theory of gravity is possible and whether there is a mediator of the gravitational in-
275 teractions. Also, it is not known why the gravitational force is so much weaker than the other
276 forces. One possible explanation comes from a theory which predicts extra spatial dimensions
277 beyond the three we experience (e.g. the string theory). In this case, it is possible that the
278 gravitational force is shared with other dimensions and only a fraction is available in our three
279 dimensions.

281 Another mystery of the universe is its composition: it is known from the studies of the grav-
282 itational effects that our universe consists of dark energy by 68%, of dark matter by 27% and of
283 baryon matter only by 5% [6]. The dark energy resists the gravitational attraction and acceler-
284 ates the expansion of the universe, and is not detectable by any effects except gravitational. The
285 understanding of dark energy is a question of general relativity rather than particle physics. The
286 dark matter, however, likely consists of particles and therefore is a subject of particle physics.
287 It does not radiate and that is why it cannot be detected by telescopes. The nature of the dark
288 matter is not known but its constituents must be very stable to remain since the Big Bang. The
289 theory of the supersymmetry which is unifying fundamental particles and mediators predicts
290 many of new heavy particles and the lightest supersymmetric particle, the neutralino, is a good
291 candidate for dark matter.

293 One more open question is the reason for the matter/antimatter asymmetry. Matter and
294 antimatter should have been created in the same amount at the moment of the Big Bang. Most
295 of it has annihilated but because of asymmetry, there was more matter than antimatter which
296 led to the state of the Universe we observe now. There is a phenomenon of the CP-violation
297 in weak interactions observed and described which predicts the asymmetry at a certain level.
298 However, the effect of the CP-violation is not large enough to account for the observed amount
299 of the matter and, therefore, the total matter/antimatter asymmetry remains unexplained.

301 The measurement of the photon transverse momentum spectrum (P_T^γ) of the $W\gamma$ process has
302 a goal to both test the SM and search for the BSM physics. The low P_T^γ region is not expected
303 to be affected by any new physics and must agree well with the SM predictions while the high
304 P_T^γ region may indicate an existence of new physics if there is an enhancement over the SM
305 predictions. The excess would be indirect evidence of the BSM particles like supersymmetric
306 particles or additional gauge bosons which could be part of the explanation of the dark matter
307 presence or difference in magnitudes of different interactions. More theoretical details about the
308 SM description of $W\gamma$ process as well as possible BSM physics are given in Ch. 2.

₃₁₁ **2 $W\gamma$ Production Theory and Former Experimental Re-**

₃₁₂ **sults**

₃₁₃ Chapter 2 provides deeper theoretical background for the measurement of this dissertation and
₃₁₄ discusses former experimental results. The derivation of the electroweak Lagrangian is described
₃₁₅ in Ch. 2.1, including the appearance of triple gauge coupling (TGC) and quartic gauge coupling
₃₁₆ (QGC) terms. Then concepts of the cross section and the luminosity are discussed in Ch. 2.2.
₃₁₇ More specific details regarding the SM cross section of $W\gamma$ are summarized in Ch. 2.3. Possi-
₃₁₈ ble causes and potential effects of anomalous TGC (aTGC) are explained in Ch. 2.4. Finally,
₃₁₉ Ch. 2.4 lists former physics experiments which probed the same aTGC vertex which is probed
₃₂₀ in the measurement of this dissertation including measurements of exactly the same process at
₃₂₁ lower LHC beam energy.

₃₂₂

323 2.1 Electroweak Theory of the Standard Model

324 To develop a quantum field theory, we start with the Lagrangian of free fermions. In order to
325 describe a system with a conserved physical quantity, the Lagrangian is required to satisfy a
326 local invariance with respect to a certain transformation. For instance, a conservation of electric
327 charge requires local invariance under $U(1)$ transformation for the QED Lagrangian [7]. The re-
328 quirement of local invariance introduces an interaction between one or more new vector fields and
329 our free fermions. The new vector fields are mediators of an interaction conserving the physical
330 quantity. To provide a full description for a new boson field, in addition to the interaction term
331 we introduce an invariant term for the kinetic energy of the boson. Such an approach allows us
332 to derive a Lagrangian which is locally invariant with respect to a certain gauge transformation
333 and contains interacting fermions as well as interaction mediators.

334 The SM is a quantum field theory invariant under the local $SU(3)_C \times SU(2)_L \times U(1)_Y$ trans-
335 formation [7]. The SM Lagrangian includes all observed quantum fields and their interactions.

336 The part of the SM Lagrangian based on the $SU(3)_C$ symmetry is called QCD or the theory
337 of strong interactions. QCD has three types of charges which are called colors: red, blue, and
338 green. To be a subject of the strong interaction, a fermion must posses a color charge. Quarks
339 and antiquarks are such fermions. The requirement to satisfy the gauge invariance with respect
340 to $SU(3)_C$ transformations generates eight massless gluons, and the non-abelian nature of the
341 $SU(3)$ group generates self-interactions of gluons including three-gluon and four-gluon vertices.

342 The part of the SM Lagrangian based on the $SU(2)_L \times U(1)_Y$ symmetry is the founda-
343 tion of the unified theory of electroweak interactions. $SU(2)_L$ reflects transformations in the
344 weak isospin space of left-handed fermions ([1], Ch. 9) while $U(1)_Y$ reflects transformations in a
345 weak hypercharge space of all fermions. The requirement of the local gauge invariance generates
346 four massless vector bosons which are mediators of electromagnetic and weak interactions. The
347 non-abelian structure of the $SU(2)$ group generates gauge boson self-couplings the same way as
348 self-interactions of gluons appear in QCD.

349 Mass terms for the vector bosons would violate the gauge invariance of the electroweak La-
350 grangian, however it is experimentally known that the mediators of weak interactions are heavy
351 particles with masses $M_W = 80$ GeV and $M_Z = 91$ GeV. A possible solution of this discrepancy
352 is the mechanism of Spontaneous Symmetry Breaking.

353 The mechanism of Spontaneous Symmetry Breaking and the appearance of the mass terms
354 for W and Z boson is realized by introducing an additional doublet of scalar fields. After that,
355 the Lagrangian is transformed in such a way that W and Z bosons acquire masses through their
356 interactions with a new particle: the Higgs boson (H). A photon does not couple to the Higgs
357 boson remaining a massless particle and leaving QED symmetry group $U(1)$ to be unbroken.

358 The measurement in this dissertation provides a test for the electroweak sector of the SM. We
359 will retrace the steps of the derivation of the EWK part of the SM Lagrangian starting from the
360 terms for free fermions. The resulting Lagrangian accommodates electroweak gauge bosons and
361 their self-couplings. One of these self-couplings, $WW\gamma$, is the primary focus of our measurement.

362 It is experimentally known that the dynamics of weak interactions depend on particle chirality
363 ([1], chapter 4.4.1). In particular, a W boson couples to left-handed fermions and right-handed
364 antifermions only. Given different properties of left-handed and right-handed fermions, they
365 are treated differently by the electroweak theory. $SU(2)$ doublets are introduced for the wave
366 functions of left-handed fermions while $SU(2)$ singlets are introduced for the wave functions of
367 right-handed fermions. Equations 3 and 4 show wave functions for the first generation fermions.
368 Wave functions for the other two generations are constructed the same way.

$$\psi_1(x) = \begin{pmatrix} u \\ d' \end{pmatrix}_L, \psi_2(x) = u_R, \psi_3(x) = d'_R. \quad (3)$$

$$\psi_1(x) = \begin{pmatrix} \nu_e \\ e^- \end{pmatrix}_L, \psi_2(x) = \nu_{eR}, \psi_3(x) = e^-_R. \quad (4)$$

377 The state d' in Eq. 3 is a weak eigenstate which is a linear combination of the mass eigenstates
 378 of the d , c and b quark wave functions and is determined by the quark mixing matrix, V , which
 379 is also called Cabibbo-Kobayashi-Maskawa matrix [7]:

380

$$\begin{pmatrix} d' \\ c' \\ b' \end{pmatrix} = V \begin{pmatrix} d \\ c \\ b \end{pmatrix} \quad (5)$$

381 To derive the unified electroweak Lagrangian, we start with the free fermion terms:

382

$$L_0 = \sum_{j=1}^3 i\bar{\psi}_j(x)\gamma^\mu\partial_\mu\psi_j(x), \quad (6)$$

383 where γ^μ are Dirac matrices ([1], chapter 7.1) and $\psi_j(x)$ are wave functions determined by
 384 Eqs. 3 and 4.

385

386 The wave function ψ_1 changes under the $SU(2)_L \times U(1)_Y$ transformations in the following
 387 way:

388

$$\psi_1(x) \rightarrow e^{iy_1\beta}U_L\psi_1(x), \quad (7)$$

389 while the wave functions $\psi_{(2,3)}(x)$ are singlets of $SU(2)_L$ and are affected only by $U(1)$ transfor-
 390 mations:

391

$$\psi_{(2,3)}(x) \rightarrow e^{iy_{(2,3)}\beta}\psi_{(2,3)}(x). \quad (8)$$

392 The transformation in the weak isospin space is defined as $U_L \equiv e^{i\sigma_i\alpha_i/2}$ where σ_i are Pauli
 393 matrices ([1], chapter 4.2.2). Phases $\alpha_i(x)$ and $\beta(x)$ in Eqs. 7 and 8 are arbitrary functions of x ,
 394 and $y_{(1,2,3)}$ are weak hypercharges which are named analogous to electric charges in QED.

395

396 In order to satisfy the local $SU(2)_L \times U(1)_Y$ invariance, partial derivatives in Eq. 6 have to
 397 be substituted with covariant derivatives:

398

$$D_\mu\psi_1(x) = [\partial_\mu - ig\tilde{W}_\mu(x) - ig'y_1B_\mu(x)]\psi_1(x) \quad (9)$$

$$D_\mu\psi_{(2,3)}(x) = [\partial_\mu - ig'y_{(2,3)}B_\mu(x)]\psi_{(2,3)}(x) \quad (10)$$

399 where g , g' are arbitrary constants,

400

$$\tilde{W}_\mu(x) \equiv \frac{\sigma_i}{2}W_\mu^i(x) = \frac{1}{\sqrt{2}} \begin{pmatrix} \sqrt{2}W_\mu^3 & (W_\mu^1 - iW_\mu^2)/\sqrt{2} \\ ((W_\mu^1 + iW_\mu^2)/\sqrt{2} & -W_\mu^3 \end{pmatrix}, \quad (11)$$

401 B_μ , W_μ^1 , W_μ^2 , W_μ^3 are four vector bosons that arise from the requirement that the Lagrangian is
 402 invariant under local $SU(2)_L \times U(1)$ transformations.

403

404 The Lagrangian becomes:

405

$$L_0 \rightarrow L = \sum_{j=1}^3 i\bar{\psi}_j(x)\gamma^\mu D_\mu \psi_j(x) \quad (12)$$

406 To make new vector bosons physical fields it is necessary to add terms for their kinetic energies:

407

$$L_{KIN} = -\frac{1}{4}B_{\mu\nu}B^{\mu\nu} - \frac{1}{4}W_{\mu\nu}^i W_i^{\mu\nu} \quad (13)$$

408 where $B_{\mu\nu} \equiv \partial_\mu B_\nu - \partial_\nu B_\mu$, $W_{\mu\nu}^i \equiv \partial_\mu W_\nu^i - \partial_\nu W_\mu^i + g\epsilon^{ijk}W_\mu^j W_\nu^k$

409

410 Off-diagonal terms of \tilde{W}_μ are wave functions of charged vector bosons

$$W^\pm = (W_\mu^1 \mp iW_\mu^2)/\sqrt{2} \quad (14)$$

411 while W_μ^3 and B_μ are neutral fields which are mixtures of a Z boson and a photon determined by:

412

$$\begin{pmatrix} W_\mu^3 \\ B_\mu \end{pmatrix} \equiv \begin{pmatrix} \cos \theta_W & \sin \theta_W \\ -\sin \theta_W & \cos \theta_W \end{pmatrix} \begin{pmatrix} Z_\mu \\ A_\mu \end{pmatrix} \quad (15)$$

413 where θ_W is the electroweak mixing angle and A_μ is a photon field.

414

415 In order to be consistent with QED, terms involving A_μ in the electroweak Lagrangian must
416 be equal to the corresponding terms in the QED Lagrangian [7]:

417

$$L_{QED} = i\bar{\psi}(x)\gamma^\mu \partial_\mu \psi(x) - m\bar{\psi}(x)\psi(x) + qA_\mu(x)\bar{\psi}(x)\gamma^\mu \psi(x) - \frac{1}{4}F_{\mu\nu}(x)F^{\mu\nu}(x), \quad (16)$$

418 where q is electric charge of $\psi(x)$ field, $F_{\mu\nu} \equiv \partial_\mu A_\nu - \partial_\nu A_\mu$.

419

420 This requirement relates g , g' , θ_W and e as $g \sin \theta_W = g' \cos \theta_W = e$ and provides an expres-
421 sion for weak hypercharges: $y = q - t_3$, where q is the electric charge and t_3 is the z -component of
422 the weak isospin. This results in $y_1 = 1/6$, $y_2 = 2/3$, and $y_3 = -1/3$ for quarks and $y_1 = -1/2$,
423 $y_2 = 0$, and $y_3 = -1$ for leptons. A right-handed neutrino has a weak hypercharge of $y_2 = 0$.
424 It also does not have an electric charge, and as a right-handed fermion has $t_3 = 0$, therefore, it
425 does not couple to a W boson. Thus, a right-handed neutrino does not participate in any SM
426 interaction.

427

428 Writing \tilde{W}_μ in Eq. 13 explicitly, we obtain triple gauge coupling (TGC) and quartic gauge
429 coupling (QGC) terms:

430

$$L_{TGC} = -\frac{g}{4}(\partial_\mu W_\nu^i - \partial_\nu W_\mu^i)\epsilon^{ijk}W^{\mu j}W^{\nu k} - \frac{g}{4}\epsilon^{ijk}W_\mu^j W_\nu^k(\partial^\mu W^{\nu i} - \partial^\nu W^{\mu i}) \quad (17)$$

$$L_{QGC} = -\frac{g^2}{4}\epsilon^{ijk}\epsilon^{ilm}W_\mu^j W_\nu^k W^{\mu l}W^{\nu m} \quad (18)$$

431 Substituting expressions for W_μ^i and B_μ determined by Eqs. 14 and 15 into Eqs. 17 and 18 we
432 receive charged TGC and QGC terms in the Lagrangian (those involving two or four W bosons)
433 in the forms of Eqs. 19 and 22, but all neutral TGC and QGC terms (those not involving any
434 W bosons) cancel out.

435 Equation 19 involves WWZ (Eq. 20) and $WW\gamma$ (Eq. 21) interactions:

436

$$L_{TGC} = L_{TGC}^{(1)} + L_{TGC}^{(2)}, \quad (19)$$

$$L_{TGC}^{(1)} = -ie \cot \theta_W (W^{-\mu\nu} W_\mu^+ Z_\nu - W^{+\mu\nu} W_\mu^- Z_\nu + W_\mu^- W_\nu^+ Z^{\mu\nu}), \quad (20)$$

$$L_{TGC}^{(2)} = -ie(W^{-\mu\nu} W_\mu^+ A_\nu - W^{+\mu\nu} W_\mu^- A_\nu + W_\mu^- W_\nu^+ A^{\mu\nu}). \quad (21)$$

437 Equation 22 involves $WWWW$ (Eq. 23), $WWZZ$ (Eq. 24), $WWZ\gamma$ (Eq. 25), and $WW\gamma\gamma$
 438 (Eq. 26) interactions:

439

$$L_{QGC} = L_{QGC}^{(1)} + L_{QGC}^{(2)} + L_{QGC}^{(3)} + L_{QGC}^{(4)}, \quad (22)$$

$$L_{QGC}^{(1)} = -\frac{e^2}{2 \sin^2 \theta_W} (W_\mu^+ W^{-\mu} W_\nu^+ W^{-\nu} - W_\mu^+ W^{\mu+} W_\nu^- W^{-\nu}), \quad (23)$$

$$L_{QGC}^{(2)} = -e^2 \cot^2 \theta_W (W_\mu^+ W^{-\mu} Z_\nu Z^\nu - W_\mu^+ Z^\mu W_\nu^- Z^\nu), \quad (24)$$

$$L_{QGC}^{(3)} = -e^2 \cot \theta_W (2W_\mu^+ W^{-\mu} Z_\nu A^\nu - W_\mu^+ Z^\mu W_\nu^- A^\nu - W_\mu^+ A^\mu W_\nu^- Z^\nu), \quad (25)$$

$$L_{QGC}^{(4)} = -e^2 (W_\mu^+ W^{-\mu} A_\nu A^\nu - W_\mu^+ A^\mu W_\nu^- A^\nu). \quad (26)$$

440 In the measurement of this dissertation we probe $WW\gamma$ coupling (Eq. 21).

441

442 The unified electroweak Lagrangian discussed above involves kinetic energy terms for fermions
 443 and gauge bosons as well as interactions of fermions with gauge bosons, TGC, and QGC. How-
 444 ever, this Lagrangian does not contain any mass terms. Because left-handed and right-handed
 445 wave functions transform differently under the electroweak symmetry, adding fermion mass terms
 446 of $\frac{1}{2}m_f^2 \bar{\psi}\psi$ would violate the Lagrangian invariance and, therefore, fermion mass terms are for-
 447 bidden by the $SU(2) \times U(1)$ symmetry requirement. Mass terms for gauge bosons also would
 448 violate the Lagrangian invariance just as a photon mass term $\frac{1}{2}m^2 A^\mu A_\mu$ would violate $U(1)$
 449 invariance of L_{QED} [1]. Therefore, Lagrangian L in Eq. 12 contains massless particles only.

450

451 However, it is known from experiments that the Z and W bosons as well as fermions are mas-
 452 sive particles and, therefore, our theory should accommodate their masses. To introduce masses
 453 into the electroweak Lagrangian, an $SU(2)_L$ doublet of complex scalar fields $\phi(x)$ is added to
 454 the Lagrangian:

455

$$\phi(x) \equiv \begin{pmatrix} \phi^{(+)}(x) \\ \phi^{(0)}(x) \end{pmatrix} \quad (27)$$

456 By selecting a special gauge of $\phi(x)$ it is possible to spontaneously break electroweak sym-
 457 metry, generate a new scalar particle, the Higgs boson [7], and introduce mass terms for W and
 458 Z bosons and charged fermions through their couplings to the Higgs boson. The strength of the
 459 coupling constant is proportional to the square of the particle's mass, therefore, heavier particles
 460 are more likely to interact with H , and massless particles do not couple to H .

461

462 The mechanism of generating a fermion's mass involves both left-handed and right-handed
 463 components of the fermion. If our hypothesis that right-handed neutrinos do not exist is right,
 464 then the Higgs mechanism does not generate neutrino masses. However, from the experiments
 465 of neutrino oscillations, neutrinos are known to have masses even though they are orders of
 466 magnitude smaller than those of other fermions. Several hypotheses have been offered to resolve
 467 this contradiction however at the moment the mechanism for neutrinos to acquire masses remain
 468 unknown [5].

469

470 In this dissertation, we study an electroweak process $W\gamma \rightarrow l\nu_l\gamma$ and probe the TGC vertex
 471 $WW\gamma$ (Eq. 21). To do that, we measure the differential cross section of $W\gamma \rightarrow l\nu_l\gamma$ with respect

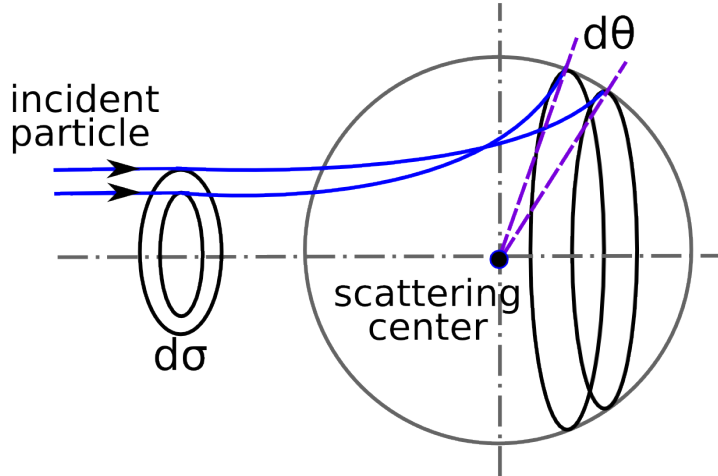
⁴⁷² to the photon transverse momentum. The concept of the cross section in particle physics is
⁴⁷³ discussed in the next chapter.

⁴⁷⁴

475 2.2 Cross Section and Luminosity

476 In this dissertation we measure the total cross section of the process $pp \rightarrow l\nu\gamma + X$ and its dif-
 477 ferential cross section in transverse momentum of the photon. A cross section in particle physics
 478 is an interaction probability per unit flux of incident particles [12]. It can be interpreted as an
 479 area which must be crossed by an incident particle in order to interact with a scattering center,
 480 or, in case of a differential cross section, area $d\sigma$ within which an incident particle must appear
 481 to be scattered off by an angle $d\theta$ (Fig. 8). The relationship between $d\sigma$ and $d\theta$ gives us the
 482 expression for a differential cross section $d\sigma/d\theta$. Integrating over $d\theta$, we obtain the total cross
 483 section σ . The cross section concept illustrated in Fig. 8 is generalized to be an effective area,
 484 and is generalized for two (or more) particle interactions rather than a light particle scattering
 485 off a stationary center.

486 The angle θ here is used only as an illustration of a concept of differential cross section. In
 487 particle physics we measure a differential cross section with respect to a parameter X which can
 488 be a parameter of one of final state particles or of a system of final state particles. For example,
 489 a cross section could be measured as a function of the transverse momentum of a final state
 490 photon P_T^γ , the invariant mass of two final state leptons m_{ll} , or even discreet observables such
 491 as the number of jets associated with the process N_{jets} .



493 Figure 8: Illustration of the differential cross section concept in the classical case.

494 In the scenario illustrated in Fig. 8, the number of particles passing through the area σ per
 495 unit time is $N = L \cdot \sigma$, where L is the flux of incident particles and is called luminosity. For
 496 colliding beams, the luminosity is determined by collisions frequency, the number of colliding
 497 particles in each beam, and beams cross sections. The cross section σ of a specific process can
 498 be determined from an experiment as $\sigma = N/L$.

499

500 A cross section can be computed theoretically using the following expression:

501

$$\sigma = \frac{W_{fi}}{F} N_{fs}, \quad (28)$$

502 where W_{fi} is a transition probability between final and initial states of the system per unit spatial
 503 volume, F is the initial flux, and N_{fs} is the density of final states ([8], chapter 4.3). The initial
 504 flux in this expression is determined as number of incident particles per unit volume multiplied

505 by their velocity and by the number of target particles per unit volume.

506

507 The formula for the cross section relevant for our measurement, two particles to three final
508 state particles scattering $1 + 2 \rightarrow 3 + 4 + 5$, is determined by the Fermi's Golden Rule [1]:

509

$$\sigma = \frac{1}{4\sqrt{(p_1 p_2)^2 - (m_1 m_2)^2}} \int |M|^2 (2\pi)^4 \delta^4(p_1 + p_2 - p_3 - p_4 - p_5) \prod_{j=3}^5 \frac{1}{2\sqrt{\bar{p}_j^2 + m_j^2}} \frac{d^3 \bar{p}_j}{(2\pi)^3}, \quad (29)$$

510 where p_i are four-momenta and \bar{p}_i are three momenta of the initial state and the final state
511 particles, m_i are masses of particles, M is the process amplitude determined by the dynamics
512 of the particles interaction. All possible momenta of the final state particles is called the phase
513 space.

514

515 During proton-proton collisions at high energy, the hard scattering process occurs between
516 partons in the protons, as discussed in Ch. 1.4. Therefore, the cross section of a process
517 $pp \rightarrow X + Y$ has two ingredients: PDFs and a partonic cross section $\sigma_{ab \rightarrow X}$. The partonic
518 cross section is described by perturbative QCD while PDFs require non-perturbative computa-
519 tions and are determined, in part, from experiments (Fig. 7). According to the QCD factorization
520 theorem [9]:

521

$$\sigma(pp \rightarrow X + Y) = \sum_{a,b} \int dx_a dx_b f_a(x_a, Q^2) f_b(x_b, Q^2) \sigma(ab \rightarrow X). \quad (30)$$

522 In the case of $W\gamma$ process, X is $l\nu\gamma$, ab are $q_i \bar{q}_j$ or $q_j \bar{q}_i$. Q^2 is the large momentum scale
523 that characterizes hard scattering, f_a and f_b are PDFs, x_a and x_b are fractions of momenta of
524 the partons. In the next sections we will discuss the computation of partonic cross sections of
525 the $W\gamma$ process and possible BSM effects.

526

2.3 Standard Model $W\gamma$ Production

A W boson in proton-proton collisions can be produced in the processes $q\bar{q}' \rightarrow W$ where q and \bar{q}' are a quark and an antiquark which have a total charge of +1 if producing a W^+ boson or -1 if producing a W^- boson. The processes $u\bar{d} \rightarrow W^+$ and $d\bar{u} \rightarrow W^-$ are the most likely to occur because u and d are valence quarks in a proton. There are twice as many u quarks in a proton as d quarks, therefore, W^+ is produced twice more frequently than W^- . Antiquarks \bar{d} and \bar{u} come from the sea $q\bar{q}$ pairs of the other proton.

Once created, a W boson decays immediately, its lifetime is $\simeq 10^{-25}$ s. In an experiment one detects its decay products rather than the W boson itself. Decay modes of a W boson include $W^\pm \rightarrow l^\pm \nu_l (\bar{\nu}_l)$ where $l^\pm = e^\pm, \mu^\pm$ or τ^\pm with branching fractions of 11% per a leptonic channel [5]. The remaining 67% account for various $W \rightarrow q\bar{q}'$ decays. In this dissertation we only consider $W^\pm \rightarrow \mu^\pm \nu_\mu (\bar{\nu}_\mu)$ and $W^\pm \rightarrow e^\pm \nu_e (\bar{\nu}_e)$ channels.

A photon can be emitted from any charged particle of the process: a quark, an antiquark, a charged lepton or a W boson (Fig. 9, top). A quark and an antiquark are initial state particles and, therefore, if one of them radiates a photon, we refer to the process as initial state radiation (ISR). A muon or an electron is a final state particle and if it radiates a photon, we call such a process final state radiation (FSR). Finally, a W boson is a gauge boson and if it radiates a photon, the process has a vertex with three gauge bosons: $WW\gamma$, and we call such process the triple gauge coupling (TGC). We cannot distinguish between these processes experimentally because we detect final state particles only.

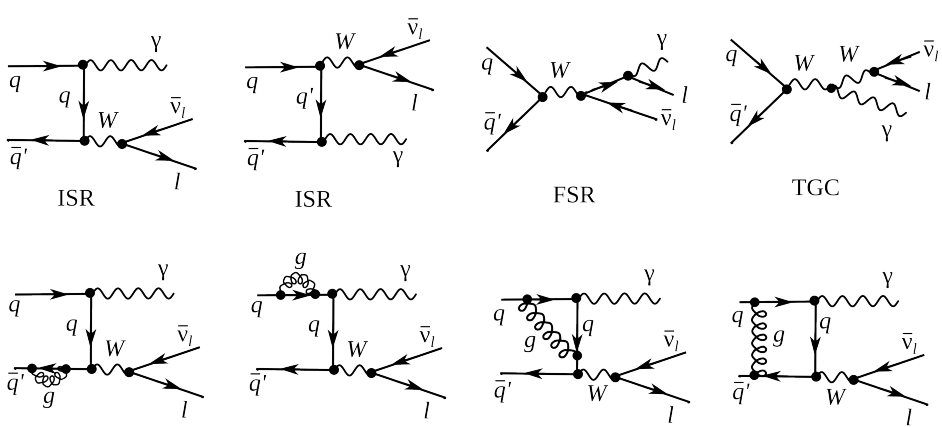


Figure 9: Feynman diagrams of $W\gamma$ production. Top: LO diagrams, bottom: several examples of NLO in QCD.

The electroweak Lagrangian is described in Chapter 2.1. It is possible to derive equations of motion from the Lagrangian for any fields involved [1]. However, in a quantum field theory equations of motion cannot be solved exactly and, therefore, the perturbative approach is used if a coupling constants is $g \ll 1$.

To represent the process graphically Feynman diagrams were invented. Also the diagrams can be used to calculate the process amplitude M in Eq. 29 because they are determined by Lagrangian terms relevant to the process. There are an infinite number of Feynman diagrams corresponding to any specific process and the total amplitude of the process is a sum of individual amplitudes of each diagram and it is not technically possible to take into account all of them. Each vertex introduces a factor in the amplitude of the process that is proportional to

561 the coupling constant. If the coupling constant is $g \ll 1$, the perturbative approach arranges
562 all the diagrams by orders of contribution, and, therefore, the Feynman diagrams with fewer
563 vertices would give a significantly larger contribution to the amplitude. In Fig. 9 examples of
564 the Leading Order (LO) and the Next-to-Leading Order (NLO) Feynman diagrams are shown
565 (top and bottom diagrams respectively).

566

567 At LO, the $W\gamma$ process is represented by four Feynman diagrams including one FSR, one
568 TGC and two ISR diagrams. Each LO diagram has three vertices. The first calculation of the
569 $W\gamma$ process with necessary expressions can be found in [14].

570

571 The NLO corrections to the amplitude of the $W\gamma$ process that are shown in Fig. 9 are QCD
572 corrections only, which include gluon loops at the same quark line and exchange of a gluon be-
573 tween two different quark lines, however, QED and weak NLO diagrams are also possible. QED
574 corrections involve radiations of extra photons by charged particles, exchange of photons be-
575 between different charged particles or a photon can be radiated and absorbed by the same charged
576 particle forming a loop. Similarly, weak corrections involve extra virtual W or Z bosons. The
577 QCD corrections are the largest among the discussed correction types because the QCD coupling
578 constant is the largest.

579

580 A theoretical cross section in particle physics is compared to a measurement result to test the
581 predictions of the model. Also the theoretical cross section is used for producing simulated data.
582 In a simulation, a large set of pp collisions resulting in a physics process of interest is modeled to
583 create a data set that mimics real data. A typical simulation consists of two parts: the generation
584 of the process and the simulation of particles paths through the detector. The first stage contains
585 a collection of events with final state particles with kinematic quantities distributed according
586 to theoretical predictions for a given process. This stage relies on the theory including the cross
587 section and also all dynamics of the process. The second stage simulates the interaction with
588 media during propagation of particles through the model of the detector as well as the response
589 of detector electronics. In its final form, a simulated dataset has the same format and content
590 of detector signals for each event as real data, and can undergo the same reconstruction and
591 analysis procedure as real data would.

592

593 The most precise theoretical $W\gamma$ cross section available is the Next-to-Next-to-Leading Order
594 (NNLO) cross section in QCD [15]. The effects of the NNLO correction over the NLO correction
595 and over the LO result are shown in Fig. 10 for the transverse mass of the final state particles
596 $m_T^{l\nu\gamma}$ and for the rapidity difference between a charged lepton and a photon $\Delta_{l\gamma}$. The NNLO and
597 NLO theoretical predictions for the photon transverse momentum p_T^γ are overlaid with 7 TeV
598 ATLAS result. The contribution from higher order corrections is estimated to be $\pm 4\%$. However,
599 the NNLO theoretical result was published only recently, in 2015, and no NNLO $W\gamma$ simulation
600 is available at this time. The simulation used in this analysis is LO + up to two hadronic jets
601 simulation which was found to give the same predictions as the NLO result.

602

603 Certain BSM theories predict an enhancement of the contribution from the TGC diagram
604 over the SM prediction. The discussion of these BSM effects and how they affect the $W\gamma$ process
605 takes place in Ch. 2.4.

606

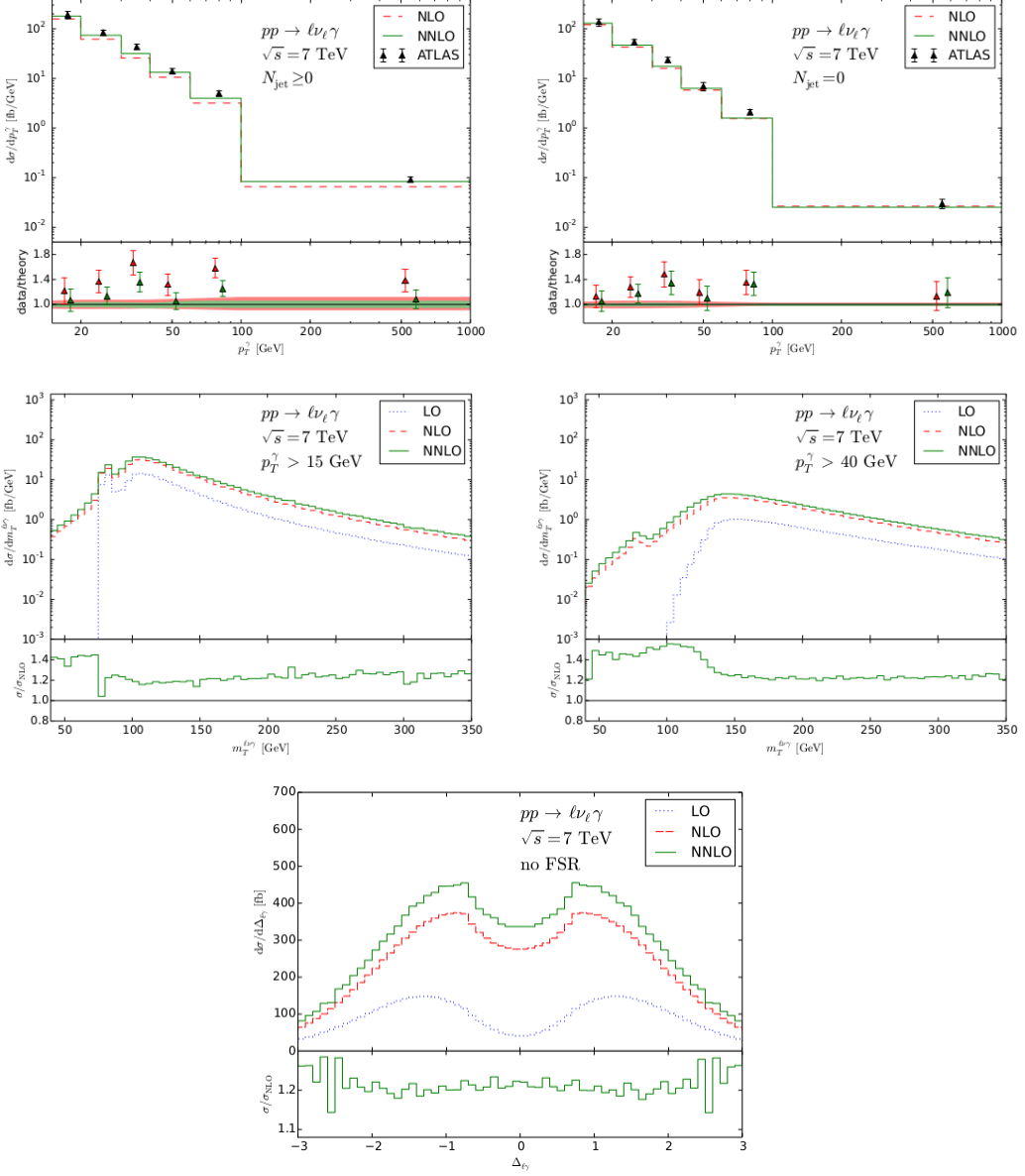


Figure 10: Theory spectra. Top: NLO and NNLO p_T^γ spectra of $W\gamma \rightarrow l\nu\gamma$ at $\sqrt{s} = 7$ TeV overlaid with ATLAS data for $N_{jet} \geq 0$ (left) and $N_{jet} = 0$ (right). Middle: LO, NLO and NNLO $m_T^{l\nu\gamma}$ spectra of $W\gamma \rightarrow l\nu\gamma$ at $\sqrt{s} = 7$ TeV for $P_T^\gamma > 15$ GeV (left) and $P_T^\gamma > 40$ GeV (right). Bottom: LO, NLO and NNLO $\Delta_{l\gamma}$ spectra of $W\gamma \rightarrow l\nu\gamma$ at $\sqrt{s} = 7$ TeV.

2.4 Anomalous $W\gamma$ Production

Most BSM physics theories predict the existence of particles with masses lying beyond the discovered energy range. If their masses are not accessible even at the accelerators with the highest energies, the direct detection of such particles is not possible. However, loops of heavy particles can affect diagrams of productions of lighter particles. They would give additional contributions to TGC and QGC couplings and, therefore, to the amplitudes to the processes involving TGC and QGC productions. There would be a different number of events produced in the process than one would expect based on SM predictions as shown in Fig. 12.

TGC and QGC couplings can be probed by precision measurements of SM processes of diboson and triboson productions because these processes can occur through TGC and QGC. TGC and QGC are represented by vertices with three and four bosons (Fig. 11). As discussed in Ch. 2.1, charged TGC and QGC are possible at tree level in the SM while neutral TGC and QGC are not.

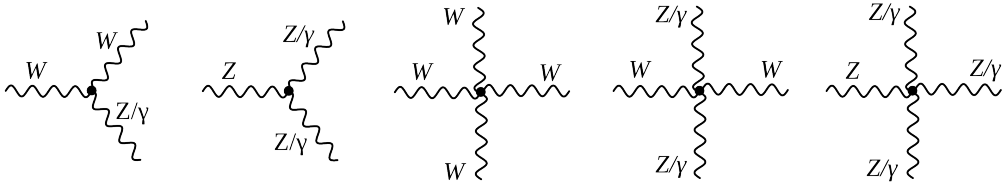


Figure 11: Charged TGC (first), neutral TGC (second), charged QGC (third and fourth), and neutral QGC (fifth) vertices.

To account for the effects from the potential loops of heavy particles, we introduce an effective Lagrangian with arbitrary values of coupling constants which can be reduced to the SM Lagrangian if these constants would have their SM values. Introducing the effective Lagrangian makes searches model-independent because we do not specify particles that form the loops but instead just check whether there is a deviation from the SM prediction in measured observables.

In $W\gamma$ measurement we can probe $WW\gamma$ vertex. The most general Lorentz invariant Lagrangian terms of $WW\gamma$ interaction takes the following form [17]:

$$iL_{eff}^{WW\gamma} = iL_{eff(1)}^{WW\gamma} + iL_{eff(2)}^{WW\gamma} + iL_{eff(3)}^{WW\gamma}, \quad (31)$$

where

$$iL_{eff(1)}^{WW\gamma} = e[g_1^\gamma A^\mu (W_{\mu\nu}^- W^{+\nu} - W_{\mu\nu}^+ W^{-\nu}) + \kappa_\gamma W_\mu^+ W_\nu^- A^{\mu\nu} + \frac{\lambda_\gamma}{m_W^2} A^{\mu\nu} W_\nu^{+\rho} W_{\rho\mu}^-], \quad (32)$$

$$iL_{eff(2)}^{WW\gamma} = e[i g_5^\gamma \epsilon_{\mu\nu\rho\sigma} ((\partial^\rho W^{-\mu}) W^{+\nu} - W^{-\mu} (\partial^\rho W^{+\nu})) A^\sigma + i g_4^\gamma W_\mu^- W_\nu^+ (\partial^\mu A^\nu + \partial^\nu A^\mu)], \quad (33)$$

$$iL_{eff(3)}^{WW\gamma} = e[\frac{\tilde{\kappa}_\gamma}{2} W_\mu^- W_\nu^+ \epsilon^{\mu\nu\rho\sigma} A_{\rho\sigma} - \frac{\tilde{\lambda}_\gamma}{2m_W^2} W_{\rho\mu}^- W_\nu^{+\mu} \epsilon^{\nu\rho\alpha\beta} A_{\alpha\beta}], \quad (34)$$

where e is the absolute value of the electron charge, A^μ is the photon field, $W^{\pm\mu}$ are the fields of the W^\pm bosons, $W_{\mu\nu} = \partial_\mu W_\nu - \partial_\nu W_\mu$, $A_{\mu\nu} = \partial_\mu A_\nu - \partial_\nu A_\mu$, m_W is the mass of the W boson,

635 g_1^γ , κ_γ , λ_γ , g_5^γ , g_4^γ , $\tilde{\kappa}_\gamma$, and $\tilde{\lambda}_\gamma$ are constants.

636

637 Despite seven constants in the extended Lagrangian, only λ_γ and κ_γ are considered in the
 638 aTGC searches. The rest of the constants are fixed to their SM values based on the following
 639 considerations. The constants $g_1^\gamma = 1$ and $g_5^\gamma = 0$ are fixed to make the Lagrangian obey the
 640 electromagnetic gauge invariance for the on-shell photons. The non-zero value of g_5^γ also violates
 641 C and P conservations, and non-zero values of g_4^γ , $\tilde{\kappa}_\gamma$, $\tilde{\lambda}_\gamma$ violate the CP conservation law. Such
 642 violation parametrizations are not considered in charged TGC measurements, thus, constants
 643 g_4^γ , $\tilde{\kappa}_\gamma$, and $\tilde{\lambda}_\gamma$ are fixed to zero.

644

645 The SM values of λ_γ and κ_γ are $\lambda_\gamma = 0$ and $\kappa_\gamma = 1$. For convenience, the deviation from the
 646 SM value is introduced $\Delta\kappa_\gamma \equiv \kappa_\gamma - 1$. These two parameters are tested in $WW\gamma$ aTGC searches
 647 because non-zero values of these parameters would not violate any fundamental law.

648

649 The most significant effects of aTGC would appear at high energy scales. Figure 12 shows
 650 this effect in P_T^γ spectrum of 7 TeV $W\gamma \rightarrow \mu\nu\gamma$ measurement. As seen in Fig. 12, the spectrum
 651 with non-zero values of aTGC constants at low P_T^γ coincides with the SM prediction but for
 652 higher P_T^γ the disagreement appears.

653

654 A common approach to aTGC searches is to measure the spectrum of a kinematic parameter
 655 highly correlated with the energy of a final state particle or a system of final state particles. For
 656 $W\gamma$ process, the most sensitive variable is P_T^γ . Examining this spectrum allows us to probe and
 657 constrain aTGC coupling constants. Chapter 2.4 reviews the experimental results to date on
 658 constraining aTGC coupling constants of the $WW\gamma$ vertex.

659

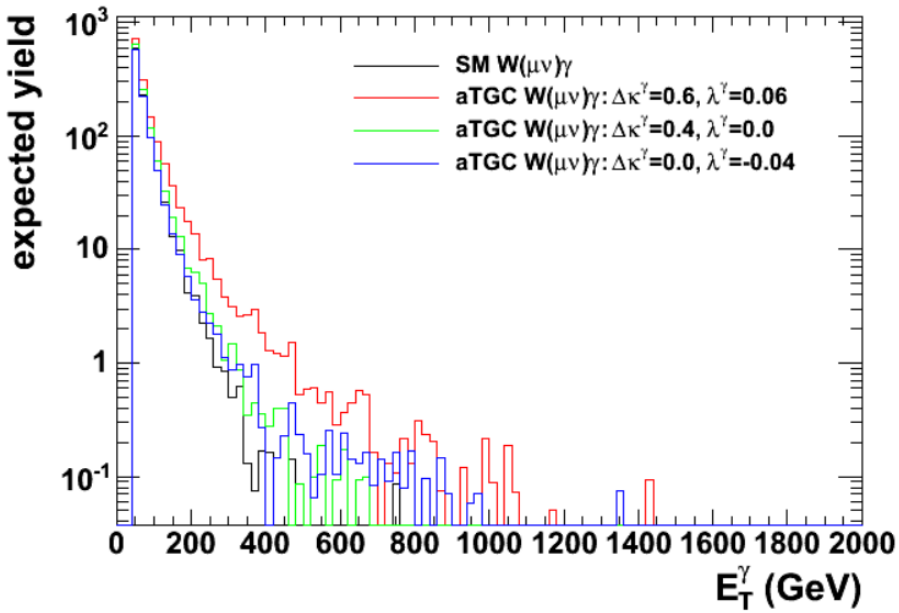


Figure 12: Distributions of P_T^γ in simulated $W\gamma \rightarrow \mu\nu\gamma$ events with different values of aTGC constants at LHC energy of $\sqrt{s} = 7$ TeV. Source of figure: [18].

aTGC parameters of the $WW\gamma$ vertex can be probed in measurements of $W\gamma$, WW , WZ processes. Limits on the $\Delta\kappa_\gamma$ and λ_γ constants obtained by different experiments are summarized in Fig. 13. The summary includes the combination results from D0 [19] and LEP [20] as well as results of several individual measurements by ATLAS and CMS including $W\gamma$ at $\sqrt{s} = 7$ TeV [21], [22], WW at $\sqrt{s} = 7$ and 8 TeV [23], [24], [25], and WV at $\sqrt{s} = 7$ and 8 TeV [26], [28] measurements.

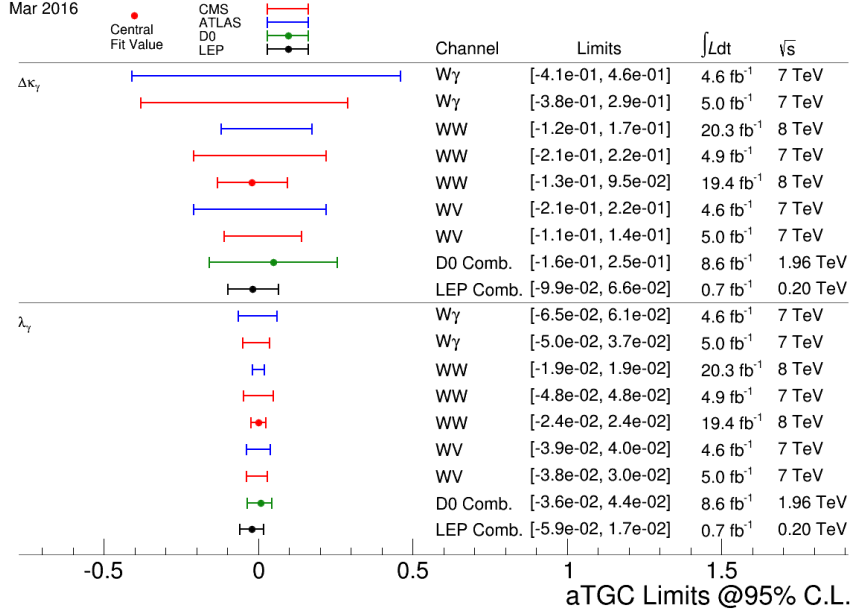


Figure 13: Summary of limits on the $WW\gamma$ aTGC coupling constants. Figure from [27].

The most recent measurements of $W\gamma$ production were performed by CMS [22] and ATLAS [21] collaborations with pp collisions at $\sqrt{s} = 7$ GeV collected in 2011. Both collaborations considered two channels: $W\gamma \rightarrow \mu\nu\gamma$ and $W\gamma \rightarrow e\nu\gamma$.

Diboson processes are rare in pp -collisions and analysts have to filter out events of their interest from many processes which are more likely to happen. To do that, a variety of selection criteria are applied which reject most of the background events to increase the signal fraction in the selected sample as much as possible. However, even after all possible selection criteria are applied, the majority of selected events are still background events and it is not possible to reduce the background any further without also significantly reducing signal.

The major source of such irreducible background is the fake photon background where hadronic jets are misidentified as photons. Such events originate mostly from $W+jets$, but $Z+jets$ and $t\bar{t}+jets$ events contribute to this source of background as well. In the electron channel there is one more significant background that is the fake photon background where electron is misidentified as a photon. Such events are coming from $Z+jets$ events. For the muon channels this background is small. Other sources of backgrounds for both channels include real- γ , fake lepton + real photon and fake lepton + fake photon backgrounds. The major source of real- γ background is the $Z\gamma$ process where a final state lepton and a photon mimics the $W\gamma$ final state. Fake lepton + real photon background originates from the $\gamma+jets$ process where a jet is misidentified as a lepton. Fake lepton + fake photon backgrounds come from dijet and multijet events where one of the jets is misidentified as a lepton and the other one is misidentified as a photon. The probability of a jet to be misidentified as a lepton is very small, therefore fake lepton + real photon and fake lepton + fake photon backgrounds are negligible.

691 Both channels provide measurements of P_T^γ spectra because this variable is the most sensitive
 692 to the potential aTGC. The P_T^γ spectra of the selected events in data superimposed with selected
 693 events in the simulation of the signal and estimated background contribution for the muon and
 694 electron channels are shown in Fig. 14 for CMS and in Fig. 15 for ATLAS measurement. Both
 695 measurements show a good agreement between data and the simulation.
 696

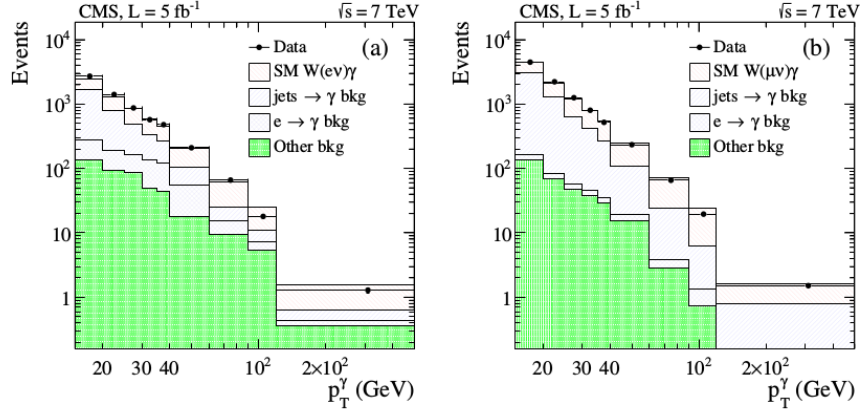


Figure 14: The distribution of the p_T^γ of $W\gamma$ candidates in the analysis of 7 TeV CMS data. Data vs signal MC + background estimates. Left: $W\gamma \rightarrow e\nu\gamma$, right: $W\gamma \rightarrow \mu\nu\gamma$ [22].

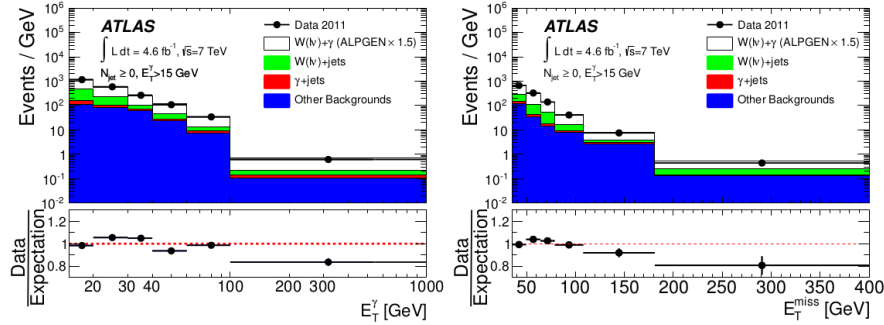


Figure 15: The distribution of the photon transverse momentum (left) and missing transverse momentum (right) of $W\gamma$ candidates in the analysis of 7 TeV ATLAS data. Data vs signal MC + background estimates [21].

698 The phase space restrictions of $W\gamma$ measurements come from the considerations of the detector
 699 acceptance, reducing heavily background-dominated regions and theoretical considerations
 700 such as to avoid divergence of the cross section and to reduce ISR and FSR contributions to the
 701 cross section.

702 CMS provides measurements of the P_T^γ spectrum, the total cross section within the phase
 703 spaces of $\Delta R > 0.7$, $P_T^\gamma > 15$ GeV, $P_T^\gamma > 60$ GeV and $P_T^\gamma > 90$ GeV.

704 ATLAS, in addition to the P_T^γ spectrum, total cross section and limits, provides the dif-
 705 ferential cross section and cross section with different number of associated jets. The phase

708 space restrictions for ATLAS measurement include requirements on charged lepton kinematics
709 $P_T^l > 25 \text{ GeV}$, $|\eta_l| < 2.47$, requirements on the transverse momentum of a neutrino $P_T^\nu > 35 \text{ GeV}$,
710 photon kinematics $P_T^\gamma > 15 \text{ GeV}$, $|\eta^\gamma| < 2.37$, photon isolation fraction $\epsilon_h^P < 0.5$ and lepton-
711 photon separation $\Delta R(l, \gamma) > 0.7$. For the differential cross section in number of associated jets,
712 the requirements on jets kinematics and jets separation from leptons and photons are also ap-
713 plied: $E_T^{jet} > 30 \text{ GeV}$, $|\eta^{jet}| < 4.4$, $\Delta R(e/\mu/\gamma, jet) > 0.3$. No evidence of new physics is observed.

714

715 The estimated cross sections with any number of associated jets for $P_T^\gamma > 15 \text{ GeV}$ are

716

$$\sigma(pp \rightarrow W\gamma \rightarrow l\nu\gamma) = 37.0 \pm 0.8 \text{ (stat.)} \pm 4.0 \text{ (syst.)} \pm 0.8 \text{ (lumi.) pb} \quad (35)$$

717 and

718

$$\sigma(pp \rightarrow W\gamma \rightarrow l\nu\gamma) = 2.77 \pm 0.03 \text{ (stat.)} \pm 0.33 \text{ (syst.)} \pm 0.14 \text{ (lumi.) pb} \quad (36)$$

719 for CMS and ATLAS respectively. The results agree with NLO MCFM predictions of $31.81 \pm$
720 1.8 pb for the phase space used by CMS and of $1.96 \pm 0.17 \text{ pb}$ for the phase space used by ATLAS.

721

722 In addition to the cross sections, both CMS and ATLAS provide limits on aTGC coupling
723 constants $\Delta\kappa_\gamma$ and λ_γ . To do that, samples with non-zero aTGC coupling constants are gen-
724 erated, run through the whole reconstruction and selection procedures, and compared to the
725 measured results of P_T^γ spectra. The results on one-dimensional limits are quoted in Fig. 13
726 while the results on two-dimensional limits can be found in [21], [22].

727

728 In this dissertation we are measuring total and differential $d\sigma/dP_T^\gamma$ cross section. While the
729 aTGC limits are not derived in this dissertation, the measured differential cross section can be
730 used to derive them. The measurement details and results are described in Chapter 5.

731

732 **3 Experimental Setup**

733 3.1 Large Hadron Collider

734 The Large Hadron Collider (LHC) [31], [32], [33] is the largest particle accelerator and the most
735 ambitious particle physics research facility ever built. The LHC is placed into a tunnel originally
736 built for the LEP accelerator. The LEP was decommissioned to make room for the LHC. The
737 tunnel is about 27 km in circumference, located at the Swiss-French boundary up to 100 meters
738 undergroud.

739 Before entering LHC, particle beams are going through several stages of the acceleration and
740 the LHC is the last element of the chain of the CERN's accelerator complex (Fig. 16). Protons
741 are extracted from hydrogen atoms, are accelerated by Linac2 to energies of 5 MeV, then injected
742 into the Proton Synchrotron Booster (PSB) where they reach energies of 1.4 GeV. After that
743 protons are sent to PS and Super PS (SPS) where they are accelerated up to 25 GeV and 450 GeV
744 respectively. Finally, protons enter the LHC and are accelerated to reach their collision energies
745 of several TeV per beam. Besides protons, the complex also accelerates and collides lead ions
746 however in this dissertation we analyze data from proton-proton collisions only and, therefore,
747 are not discussing lead ion collisions.

748 Main goals of LHC were to detect the SM Higgs boson if it existed and to search for evidences
749 of BSM physics which may give a clue on understanding the phenomena including but not limited
750 to the dark matter, the matter-antimatter asymmetry, the nature of the gravitational force. Six
751 detectors are installed at the LHC to detect particles and perform the relevant measurements.
752 There are general purpose detectors ATLAS and CMS, there is LHCb which specializes of the
753 physics of B-mesons, and ALICE which is designed to detect products of heavy ion collisions. In
754 addition, there are two relatively small detectros: LHCf and TOTEM which are installed close
755 to the ATLAS and CMS collision points respectively.

756 The design energy of the LHC is 7 TeV per beam however several lower energy points were
757 and are being probed. In 2010-2011 the LHC operated at energy of 3.5 TeV per beam which was
758 already higher than energy of any other collider. In 2012 the energy increased up to 4 GeV. In
759 2013-2014 the LHC was shut down for upgrades. Collisions were restarted at 6.5 TeV in 2015
760 and the LHC is still operating at this energy in 2016.

761 All important measurements performed at lower energies are also repeated at higher energies
762 because the ability to probe higher energy scales increases our chances for a discovery and even
763 if no deviations from the known physics are found at a given energy point, the discovery is still
764 possible to happen as we go higher in the energy.

765 The greatest achievement by the LHC today is the discovery of the Higgs boson in 2012 by
766 the CMS [3] and the ATLAS [4] collaborations in 2012.

767 While different BSM searches have been constituting a significant part of the LHC physics
768 program since the beginning of its operation, no deviations from the SM were found by any of
769 the experiments. The searches continue with higher beam energies and larger amount of data.

770 In addition to the beam energy, there are many other collider parameters. A brief summary
771 of them is available in Tab. 2. One of the most important parameters of an accelerator is the
772 ability to produce a large number of interesting collisions which is determined by the luminosity.
773 The instantaneous luminosity is determined by the following expression [5]:

$$774 L = f \frac{n_1 n_2}{4\pi \sigma_x \sigma_y}$$

775 where n_1 and n_2 are numbers of particles in colliding bunches, f is a frequency of collisions,
776 σ_x and σ_y are beam sizes in horizontal and vertical directions. To determine the integrated
777 luminosity, one has to integrate the instantaneous luminosity over time:

788 $L_{int} = \int L dt$

789

790 The luminosity of the LHC is also higher than of any previously existed collider. The integrated
 791 luminosity of the LHC for different years of the operation are shown in Fig. 17. Run periods of
 792 LHC in 2010-2012 refer to Run I of the LHC operation. While working on energy of $\sqrt{s} = 7$ TeV,
 793 LHC delivered 44.96 pb^{-1} and 6.1 fb^{-1} of data in 2010 and 2011 year respectively. In 2012 the
 794 working energy of LHC was $\sqrt{s} = 8$ TeV, and the integrated luminosity was $L_{int} = 23.3 \text{ fb}^{-1}$.
 795 After a long shutdown, LHC was upgraded for Run II, to operate on $\sqrt{s} = 13$ TeV in 2015 and
 796 delivered 4.22 fb^{-1} of data by the end of 2015. In 2016 LHC continues operation on $\sqrt{s} = 13$ TeV
 797 and by the end of September the integrated luminosity already exceeded a value of 30 fb^{-1} [37].

798

799 CHECK INFORMATION FOR THE WHOLE 2016...

800 POSSIBLY UPDATE PLOT...

801

802 The measurement of this dissertation is performed at the energy of 4 TeV per beam or at
 803 the center of mass energy $\sqrt{s} = 8$ TeV with 19.6 fb^{-1} of data. The same process was measured
 804 at $\sqrt{s} = 7$ TeV with about four times less amount of data by both CMS and ATLAS. These
 805 measurements are discussed in greater details in Ch. 2.4.

806

Table 2: Main parameters of LHC [31]

Circumference	27 km
Dipole operating temperature	1.9 K
Number of magnets	9593
Number of main dipoles	1232
Number of main quadrupoles	392
Number of RF cavities	8 per beam
Nominal energy, protons	7 TeV
Nominal energy, lead ions	2.76 TeV per nucleon
Peak magnetic dipole field	8.33 T
Min. distance between bunches	7 m
Design luminosity	$10^{34} \text{ cm}^{-2} \text{ s}^{-1}$
No. of bunches per proton beam	2808
No. of protons per bunch (at start)	1.1×10^{11}
No. of collisions per second	600 millions

CERN's Accelerator Complex

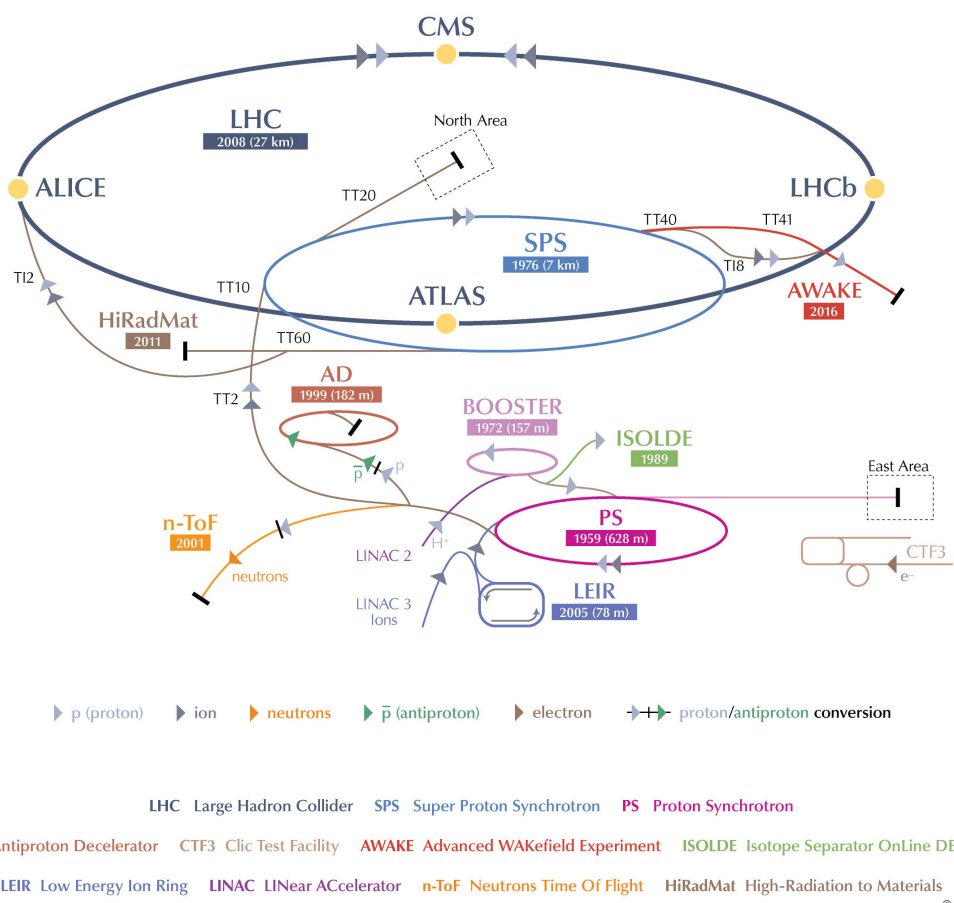


Figure 16: CERN's accelerator complex. Source of the figure: [34].

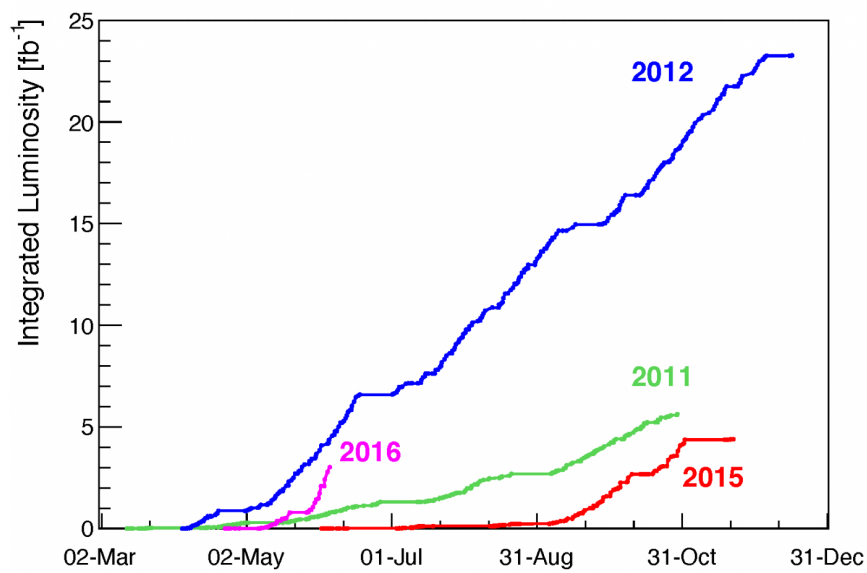


Figure 17: LHC integrated luminosity by year. Source of the figure: [35].

3.2 Compact Muon Solenoid

3.2.1 Introduction

The CMS is a general-purpose detector designed for detecting various highly energetic particles which are being produced in pp collisions at the LHC. The CMS has a broad program with goals of direct and indirect searches of the BSM physics including but not limited to supersymmetric particles. Its main feature is a huge magnet to create a magnetic field of 4T to curve charged particles in the tracking system and of 2T outside to curve muons in the muon system.

The CMS detector is a cylindrically symmetric with a colliding beam as a central axis. Cartesian, cylindrical and spherical coordinates are all used to describe the CMS geometry, depending on the context. The x -axis of the CMS points towards the center of the LHC while the y -axis points vertically up. The direction of the z -axis corresponds to the counterclockwise direction of the LHC beam (Fig. 18, left). Cylindrical coordinates are defined as $r = \sqrt{x^2 + y^2}$, $\phi = \arctan(y/x)$. Instead of the polar angle θ , it is more convenient to use the pseudorapidity $\eta = -\ln \tan \theta/2$. A pseudorapidity ranges from $\eta = -\infty$ to $\eta = +\infty$ for directions parallel to the beam axis with the value of $\eta = 0$ for a direction perpendicular to the beamline. This variable is convenient for measurements because a distribution of a massless particle in η is nearly flat. The acceptance of the CMS in η is limited and varies from $|\eta| = 2.4$ to $|\eta| = 5.0$ depending on a subdetector.

826

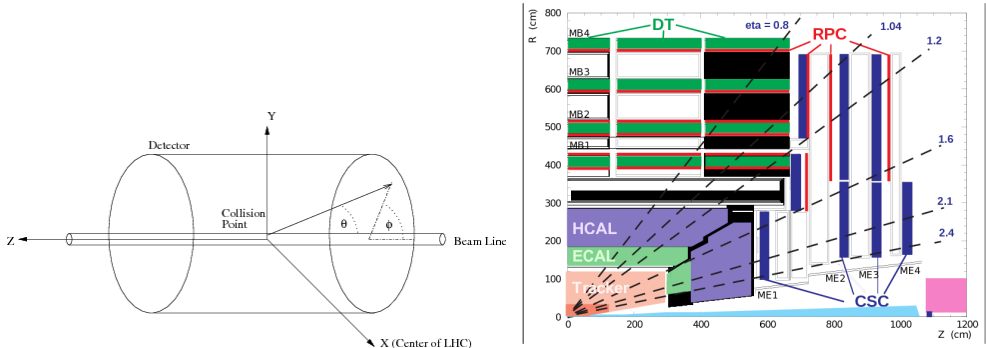


Figure 18: Left: CMS coordinate system. Right: pseudorapidity ranges for different CMS subdetectors.

The detector consists, from inner to outer layer, of a tracking system, an electromagnetic calorimeter (ECal), a hadronic calorimeter (HCal), a magnet and a muon system. Having the tracking system, ECal and HCal inside of a large solenoid makes the detector compact. A segment of a CMS slice in $r - \phi$ plane is shown in Fig. 19.

When a heavy particle is produced in a collision, it decays immediately, and we detect its long-living decay products including an electron, a photon, a muon, a neutral hadron or a charged hadron. Depending on the trace left by a particle in different subdetectors we can identify a particle. Electrons and positrons leave curved tracks in the tracking system and then induce showers in the electromagnetic calorimeter (ECal). Photons induce the same electromagnetic showers in ECal however, as neutral particles, they do not leave tracks in the tracking system. Hadrons normally travel through the ECal undisturbed and induce a hadronic shower in the hadronic calorimeter (HCal). Charged and neutral hadrons can be distinguished from each other by checking whether they leave a track in the tracking system or not. Muons are the only particles which penetrate through the ECal, the HCal and the magnet and leave tracks in the CMS muon system. Neutrinos are not detected by CMS.

843

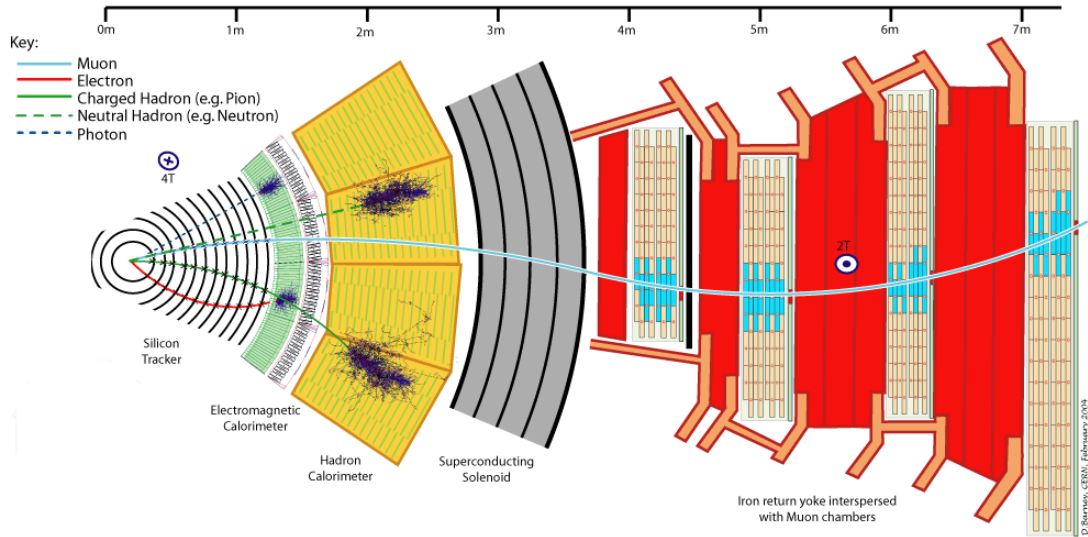


Figure 19: CMS slice.

844 All subdetectors are important for the $W\gamma$ measurement and the remainder of this chapter
 845 describes the subdetectors in greater details. Muons and electrons which we have as final state
 846 particles are both affected by CMS magnetic field allowing the tracking system and the muon
 847 system to measure their trajectory parameters and momenta. In this dissertation we use the
 848 information of the primary vertex determined by the tracking system to select our events. Also
 849 the tracker provide us the information about electrons trajectories and momenta in the electron
 850 channel and distinguishes between electrons and photons.
 851

852 3.2.2 Magnet

853 A magnetic field in a particle detector is necessary to measure momenta of charged particles
 854 by track curvatures. The higher the momentum is, the less a particles's path is affected by the
 855 magnetic field. In CMS it is done in the tracking system for all charged particles and in the
 856 muon system for muons.
 857

858 The CMS magnet is placed between layers of HCal and a muon system. It creates a magnetic
 859 field of 4T inside the magnet, for the tracking system, and 2T outside the magnet, for the muon
 860 system. It is necessary to have stronger field in the tracking system because a density of tracks
 861 is much higher there than in the muon system and also the tracking system is much smaller and,
 862 therefore, more significant curvature is necessary to measure the momentum with high precision.
 863

864 The magnet is made of superconducting wires. An electric current flowing in the wires creates
 865 a uniform field inside the solenoid and also provides a magnetic field of a certain configuration
 866 outside the solenoid.
 867

868 3.2.3 Tracking System

869 The tracking system measures track geometry including particles trajectories and locations of
 870 primary and secondary vertices and momenta of charged particles. It needs to disturb particles

as little as possible so that they can pass through. Therefore, just a few measurements must be enough to reconstruct the track. The accuracy of a measurement of each hit is $10 \mu\text{m}$.

The tracking system consists of silicon pixels and silicon strips (Fig. 20). Collision tracks start at the center and then cross the layers of the tracking system. Tracks are straight in $r - z$ plane and curved by the magnetic field in the $r - \phi$ plane. The acceptance of the tracker system in $r - z$ plane is geometrically limited by the absolute value of the pseudorapidity $|\eta| = 2.5$.

The pixel tracker is the closest subsystem of CMS to the collision point thus it experiences the largest particle flux: at 8 cm from the collision point the flux is about 10 million $1/(\text{cm}^2\text{s})$, and the pixel detector with its 65 millions sensors is capable to reconstruct all these tracks. It consists of three layers of cylinders in the barrel with radii of 4 cm, 7 cm and 11 cm and four disks in the endcap, two disks at each side. The tracker is designed in such a way that a single track hits multiple sensors. Then the trajectory is reconstructed based on how much charge is collected on each sensor. This allows us to reach a spacial resolution of 15-20 μm which is much smaller than a distance between sensors.

The strip tracker is placed right after the pixel tracker and occupies the detector volume up to 130 cm around the beam axis. The strip tracker consists of four parts: the tracker inner barrel (TIB), the tracker inner disks (TID), the tracker outer barrel (TOB) and the tracker endcap (TEC) as shown in Fig. 20. In the strip tracker there are over 15,000 sensitive modules with a total number of 10 million strips. Each sensitive module consists of a set of sensors, its support structure and readout elements.

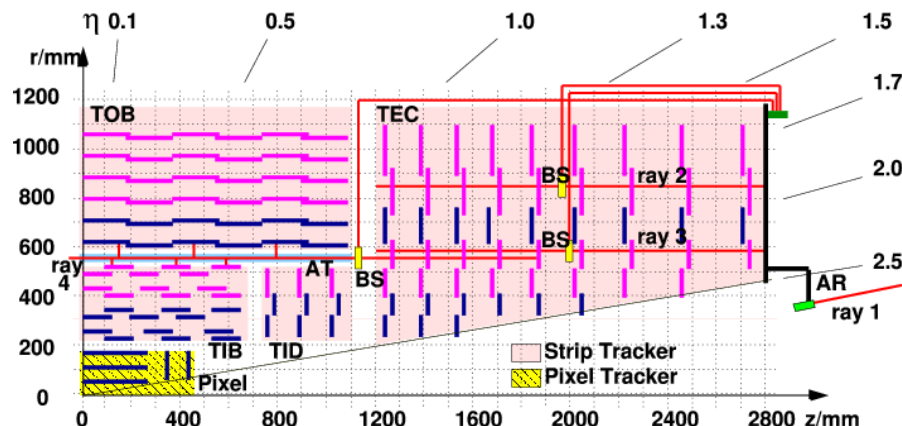


Figure 20: Slice of the CMS tracking system in $r - z$ plane.

3.2.4 Electromagnetic Calorimeter

The ECal measures energy of electrons and photons and also measures geometries of their trajectories. Electrons and photons interact with the ECal substance by inducing electromagnetic showers. Traces left by photons and electrons in the ECal are the same. To distinguish between these two particles, it is necessary to perform matching to the track in the tracking system. If there is a track, then there is an electron (or positron). If there is no track, then the particle is a photon.

The ECal is a layer between the tracking system and the HCal. It is made of high-density lead tungstate crystals arranged in a barrel section and two endcap sections. The crystals work as scintillators. When electrons and photons pass through it, it produces light proportional to the

906 particle's energy. The scintillated light then is amplified by photomultipliers producing signals
907 on sensitive elements.

908 It is important for the ECal to be able to distinguish between high energetic photons and
909 pairs of lower energetic photons e.g. from a π^0 decay. It is especially difficult in the endcap
910 sections where angle between two photon trajectories is small. ECal preshower located in front
911 of the endcaps which have much smaller granularity provide extra spacial precision. Their strips
912 are 2 mm wide compared to 3 cm wide crystals in the main volume of the ECal.
913

914

915 **3.2.5 Hadron Calorimeter**

916 The HCal is placed right after the ECal and is the last subdetector within the magnet. The
917 HCal measures energies of charged and neutral hadrons. In addition, the HCal determines the
918 track parameters. Match to the tracking system has to be done: if a matching track found, then
919 it is a charged hadron otherwise it is a neutral hadron.

920

921 The HCal consists of alternate layers of absorbers and scintillators. Hadrons hit brass or steel
922 plate of absorber producing secondary particles. When emerge into the scintillator, the particles
923 induce hadronic and electromagnetic showers and emit blue-violet light which is further shifted
924 to the green region and read out by special boxes within the HCal. The secondary hadrons pro-
925 duced during the interaction with the absorber interact with the next absorber producing more
926 showers in the next layers of scintillators and also affect the total energy deposit. All hadrons
927 must be stopped inside the layers of the HCal.

928

929 **3.2.6 Muon System**

930 Muons pass through the ECal, the HCal and the magnet without interacting. They are the only
931 particles that are registered in the muon system which is placed outside the magnet and which
932 is the largest part of CMS detector.

933

934 There are four concentric layers of muon detectors (stations) and iron return yoke between
935 them. Muons induce several hits in the muon stations which are later fitted and matched to the
936 tracking system measurements to provide the best possible resolution in the measurements of all
937 parameters of the muon's trajectory and momentum.

938

939 There are three types of muon chambers used in the CMS muon system: drift tubes (DTs),
940 cathode strip chambers (CSCs) and resistive plate chambers (RPCs). Overall, there are 1400
941 muon chambers including 250 DTs, 540 CSCs and 610 RPCs.

942

943 The system of DTs measures positions of muons in the barrel. Each DT chamber is about 2 m
944 by 2.5 m in size. It consists of 12 layers of aluminium which are arranged as groups of four. There
945 are up to 60 drift tubes in a layer. The middle group of layers measures z-coordinate and two
946 other groups determine the perpendicular coordinate.

947

948 Each drift tube is 4 cm in width, is filled with a gas and has a wire inside. When a charged
949 particle passes through the volume, it ionizes atoms and the wire receives an electric charge.

950

951 CSCs are placed in endcap regions. CSCs are arrays of anode wires crossed by copper cathode
952 strips placed in a gas volume. When a charged particle penetrates the gas volume, it ionizes the
953 gas. Electrons drift to the wires while ions move to the strips. Strips are perpendicular to wires,
954 thus, we measure two coordinates for each particle.

955

956 RPCs are parallel capacitors made of high-resistivity plastic plates with a space between
957 them filled with a gas. RPCs provide quick measurements of muon momenta and are used for

958 triggering.

959

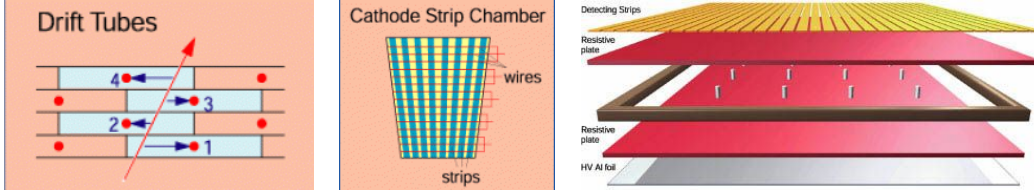


Figure 21: Components of the CMS muon system. Left to right: drift tubes, cathode strip chambers (CSCs), resistive plate chambers (RPCs).

960 3.2.7 Triggering and Data Aquisition

961 At peak luminosity, CMS experiences one billion proton-proton collisions per second which come
962 in bunches separated just by 25 ns from one other. New events come before the events from
963 the previous bunch crossing left the detector. To process the information from many different
964 collisions at the same time, data is stored in pipelines.

965

966 It is not technically possible to readout all these events. Moreover, we do not need most
967 of these events for a physics analysis because most of these events do not have a potential to
968 discover a new physics. We have resources to store about one hundred events out of one billion
969 that is why we need a trigger system that quickly decides what the best one hundred events are.

970

971 If the triggers were too loose, and we would select one hundred events too quickly, e.g., out
972 of a hundred million events, then CMS would not be able to process the rest 90% of events in a
973 given set of one billion and we would lose 90% of potentially interesting events.

974

975 If the triggers were too strict, we would select, e.g, ten events out of one billion, not one
976 hundred and lose CMS potential to store and process data by 90% which would significantly
977 reduce our chances for a discovery.

978

979 Thus, the challenge of the trigger system is to select the best one hundred events out of one
980 billion and do that fast to be able to process every single event. To achieve this goal, a two-level
981 trigger system was developed consisting from the Level 1 trigger (L1T) and the high level trigger
982 (HLT) as shown in Fig. 22.

983

984 L1T is a hardware based trigger (Fig. 23). It uses information from the ECal, HCal and
985 muon system. L1T reduces frequency of coming events from 40 MHz to 100 kHz. Events which
986 did not pass the L1T are lost forever while events which pass the L1T are temporarily stored to
987 get checked by the HLT.

988

989 HLT is a software-based trigger. It uses information from all subdetectors and runs quick
990 reconstruction and identification algorithms to determine types of particles and their kinematics.
991 It reduces the number of events to 100 Hz. Events which did not pass HLT are lost forever.
992 Events which pass HLT are arranged into appropriate datasets depending on HLT selection cri-
993 teria they passed and stored for physics analyses.

994

995 3.2.8 Particle Flow Algorithm of Event Reconstruction

996 Where to place particle reconstruction, particle flow algorithm and MET? Check other theses

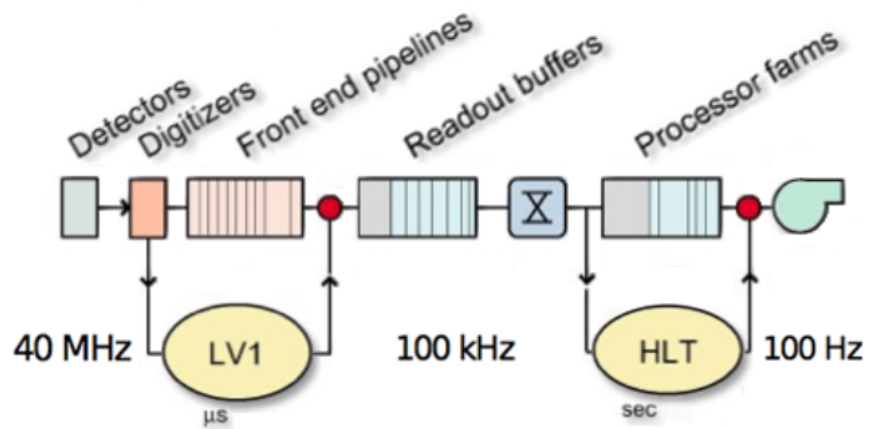


Figure 22: Two-level CMS trigger system.

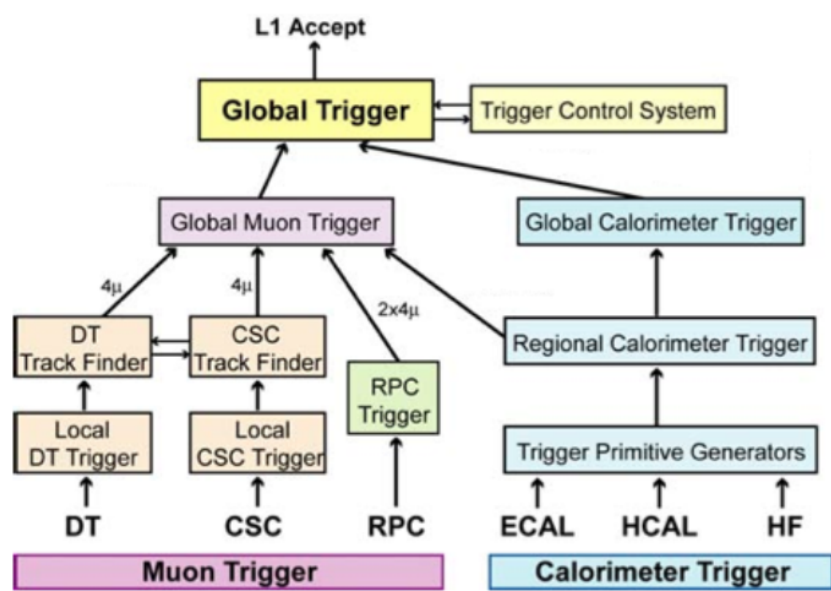


Figure 23: Level 1 CMS trigger system.

997 4 CMS Tracker Alignment

998 4.1 Algorithm

999 Why align?

1000 How to align?

1001 When align?

1002 How to check that your alignment is good?

1003

1004 A tracking system detects hits produced by a charged particle traveling through the detector.
 1005 In a presence of a constant magnetic field the particle has a helical trajectory. A reconstruction
 1006 algorithm determines the track parameters by fitting the positions of hits assuming the helix
 1007 trajectory.

1008

1009 Better hit resolution and the location uncertainty lead to better precision of a measurement
 1010 of the track parameters. The location uncertainty depends on our knowledge of the positions and
 1011 orientations in space of the tracking system modules. The hit resolution in the CMS pixel detector
 1012 is $\sim 15 \mu\text{m}$. When the modules are mounted, their positions are known with precision of $\sim 200 \mu\text{m}$.
 1013 Thus, we need to know positions of modules 20 times better than they are known when mounted.

1014

1015 The procedure of the determination of the modules locations and orientations is called the
 1016 tracker alignment. The concept of the track-based alignment can be illustrated in the example of
 1017 the alignment of a toy tracker. When a charged particle passing through a detector (Fig. 24, top
 1018 left) it crosses a toy tracker which consists of six flat equidistant modules (Fig. 24, top right). If
 1019 the modules were placed exactly at their designed positions, we would observe the hits exactly at
 1020 the points where the track crosses modules at the points of ideal geometry (Fig. 24, middle left).
 1021 However, in a reality the positions and tilts of the modules are different from ones suggested by
 1022 the ideal geometry (Fig. 24, middle right). Hits, indeed, are recorded at the places where mod-
 1023 ules are actually mounted, not at the design ideal places (Fig. 24, bottom left). If we assumed a
 1024 tracker to be ideal and a track to be smooth, we would see that our hits are off-track (Fig. 24,
 1025 bottom right). So, we recalculate positions of the modules so that all the hits are laying on the
 1026 same smooth track (Fig. 25, top left). But these recalculated positions still do not coincide with
 1027 the actual positions (Fig. 25, top right). Then we record more and more tracks (Fig. 25, middle
 1028 left and right). We take into account them all and determine the alignment parameters with
 1029 necessary precision (Fig. 25, bottom left and right).

1030

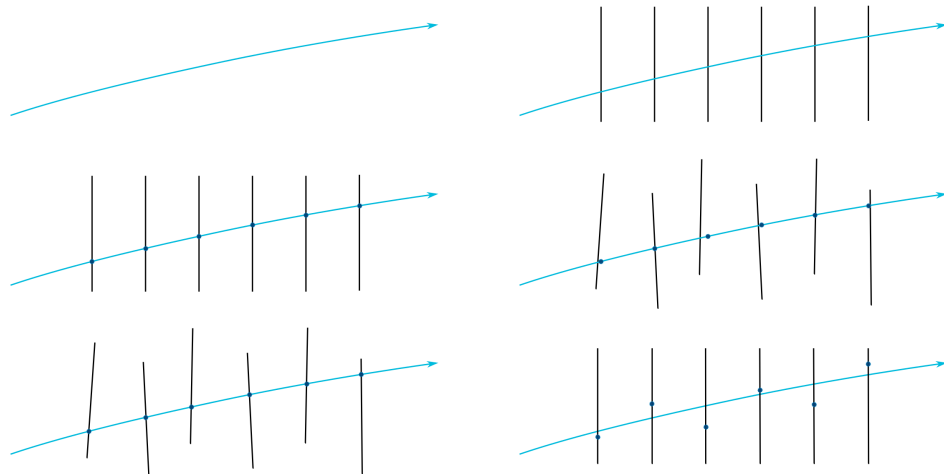


Figure 24: The alignment of a toy tracker, part 1.

1031

When we record a track with a not-aligned tracker, we see that the track is not smooth. But

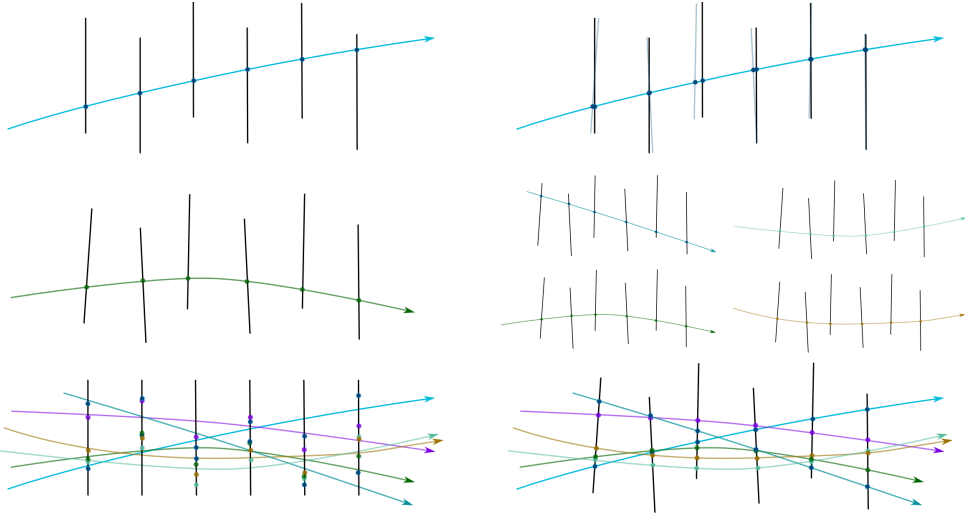


Figure 25: The alignment of a toy tracker, part 2.

that is because our knowledge of module positions is not exact. Thus, we can correct the positions assuming the track is smooth. But when we process the next track, we may find out that the positions have to be corrected again. Thus, we record many tracks and minimize residuals between measured and predicted hits.

The CMS tracker contains 1440 silicon pixel modules in PXB and PXF and 15148 silicon strip modules in TIB, TOB, TID, TEC.

The tracker alignment problem is the least squared problem. The expression to minimize is the following:

$$\chi^2(\mathbf{p}, \mathbf{q}) = \sum_j^{\text{tracks}} \sum_i^{\text{tracks}} \left(\frac{m_{ij} - f_{ij}(\mathbf{p}, \mathbf{q}_j)}{\sigma_{ij}} \right)^2 \quad (37)$$

where \mathbf{p} are parameters describing the tracker geometry, \mathbf{q}_j are parameters of the j^{th} track, $m_{ij} - f_{ij}$ are residuals, distances between the measured hit and a position predicted by the track fit, σ_{ij} is the Gaussian error of the measurement.

We can align the large substructures and individual modules with respect to their substructures. The parameters to align large substructures include their positions and orientations of the subdetectors (rotations). Thus, each subsystem is described by six parameters: three coordinates X, Y, Z and three angles α , β , γ . At the module level, we align positions and rotations with respect to the position s and angles of the corresponding large structure (Fig. 26). In addition, at the module level we align for surface deformations which are described by three parameters per sensor (Fig. 27).

A track can be described with five parameters.

We have two alignment algorithms: Millepede and HIP. Millepede performs a simultaneous fit of all alignment parameters and all track parameters while HIP perform iterative fits of alignment parameters \mathbf{p} and track parameters \mathbf{q}_j .

It is important to use different sorts of tracks for the alignment. Cosmic tracks pass through the detector vertically and do not allow us to connect different subdetectors to one another.

1062 Collision tracks originate from the collision point and go in all directions. However, those tracks
 1063 which cross TEC are all almost collinear and, therefore, it is difficult to measure z -coordinate of
 1064 TEC modules with collision tracks only.

1065

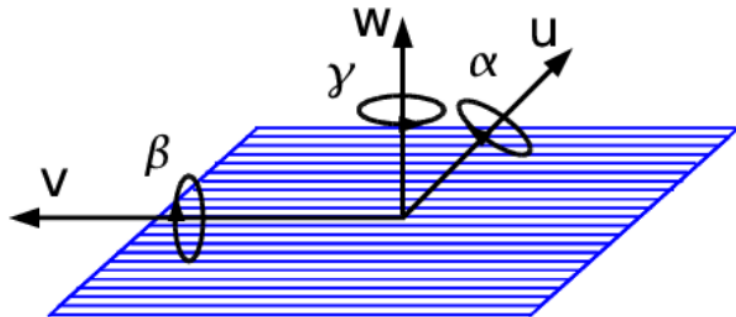


Figure 26: Alignment parameters.

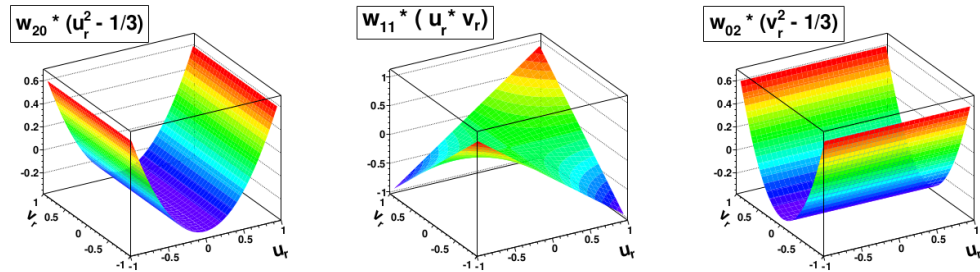


Figure 27: Surface deformations.



Figure 28: Track residuals.

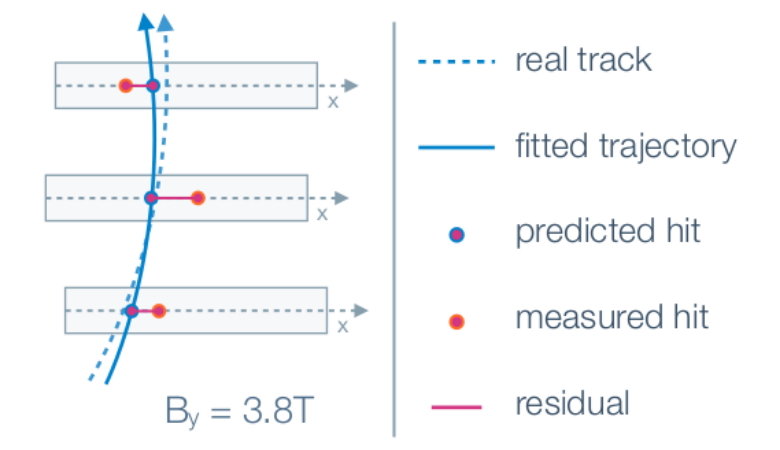


Figure 29: Track residuals.

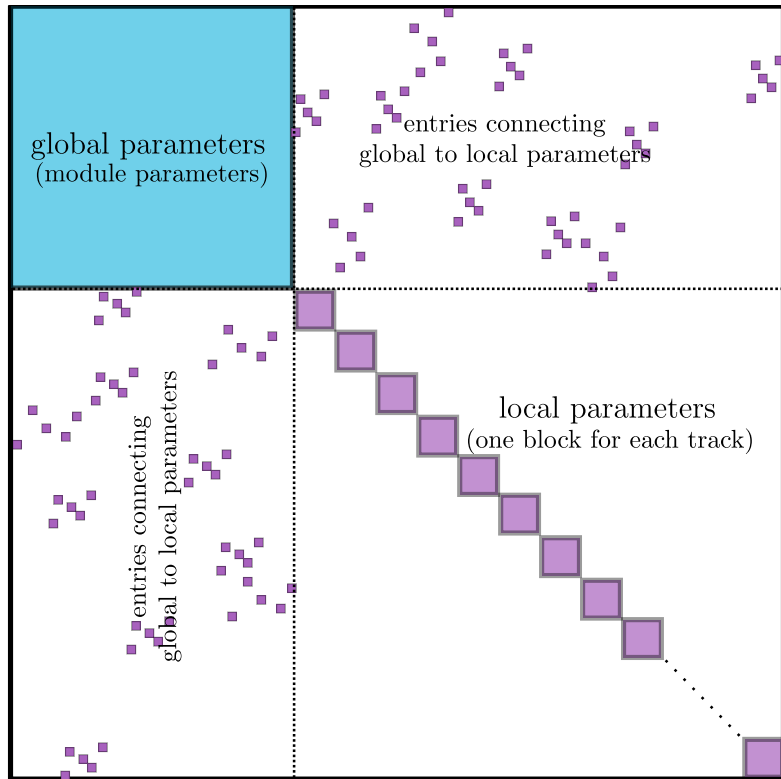


Figure 30: Track residuals.

1066 **4.2 Selected Results**

1067 CRUZET, CRAFT and first collisions of 2015

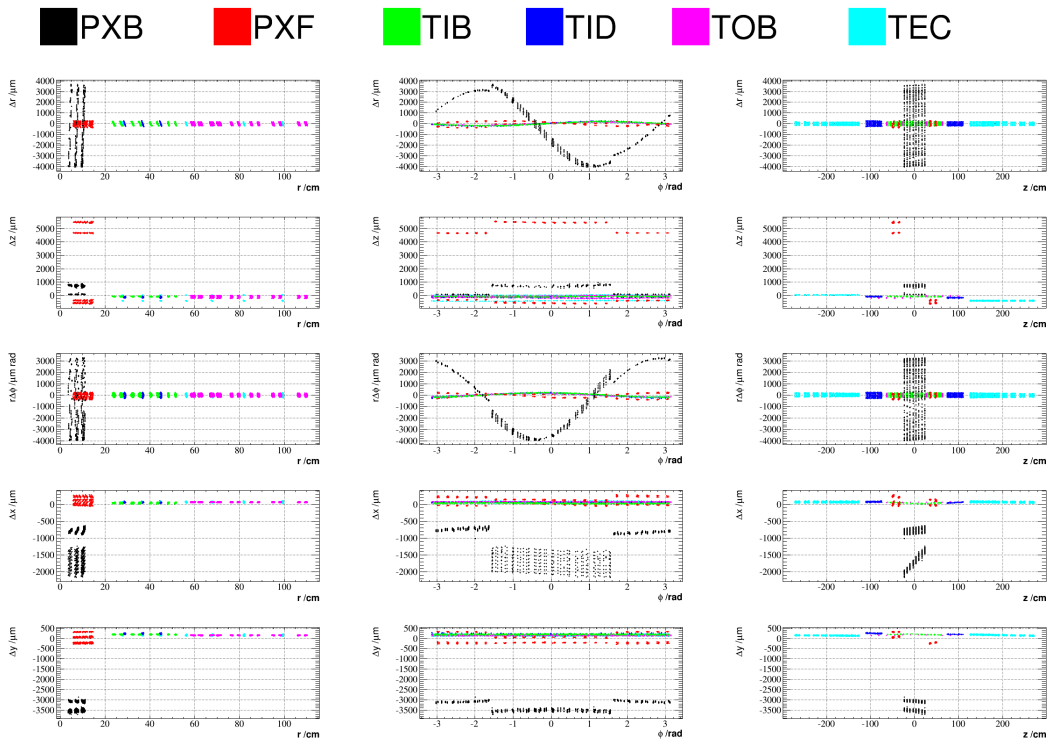


Figure 31: Geometry comparison plot of CRUZET 2015 object vs Run I.

5 $W\gamma$ Cross Section Measurement

1068 Place analysis outline here

References

- [1] Griffiths textbook
- [2] website: <http://www.isgtw.org/spotlight/go-particle-quest-first-cern-hackfest>
- [3] CMS Paper about Higgs boson discovery
- [4] ATLAS Paper about Higgs boson discovery
- [5] PDG
- [6] website: <https://science.nasa.gov/astrophysics/focus-areas/what-is-dark-energy>
- [7] Pich lectures: The Standard Model of Electroweak interactions
- [8] Halzen, Martin "Quarks and leptons"
- [9] <http://iopscience.iop.org/article/10.1088/0034-4885/70/1/R02>
- [10] Peskin, Schroeder
- [11] Lindsey's thesis (CMS Zg- ζ llg, 7 TeV)
- [12] website: https://www-d0.fnal.gov/results/publications_talks/thesis/snyder/html/node17.html
- [13] website: https://en.wikipedia.org/wiki/Cross_section_%28physics%29
- [14] LO (1969) theory paper
- [15] NNLO theory paper
- [16] NLO theory paper
- [17] aTGC paper
- [18] Senka's thesis (CMS Wg- ζ munug, 7 TeV)
- [19] D0 Combination of $W\gamma$, WW, WZ and VW using 8.6 fb-1 of 2 TeV $p\bar{p}$ collisions Phys.Lett. B718 (2012) 451-459
- [20] LEP Combination of WW and single W using 0.7 fb-1 per experiment of e^+e^- collisions at WW pair production energies arXiv:1302.3415
- [21] 7TeV Wg ATLAS paper
- [22] 7TeV Wg CMS paper
- [23] ATLAS WW using 20.3 fb-1 of 8 TeV pp collisions Submitted to JHEP
- [24] CMS WW using 4.9 fb-1 of 7 TeV pp collisions Eur. Phys. J. C 73 (2013) 2610
- [25] CMS WW using 19.4 fb-1 of 8 TeV pp collisions Submitted to EPJC
- [26] ATLAS VW ($V=W,Z \rightarrow jj$) using 4.6 fb-1 of 7 TeV pp collisions JHEP 01 (2015) 049
- [27] website: https://twiki.cern.ch/twiki/bin/view/CMSPublic/PhysicsResultsSMPaTGC#Figure_1_Limits_on_WW
- [28] CMS VW ($V=W,Z \rightarrow jj$) using 5.0 fb-1 of 7 TeV pp collisions Eur.Phys.J. C73 (2013) 2283
- [29] CMS 8 TeV WW lnlnmu
- [30] CMS 7 TeV Zg nunug
- [31] CERN brochure, <http://cds.cern.ch/record/1165534/files/CERN-Brochure-2009-003-Eng.pdf>

- 1105 [32] LHC TDR
- 1106 [33] website: <http://home.cern/topics/large-hadron-collider>
- 1107 [34] website: <http://cds.cern.ch/record/1621583/files/>
- 1108 [35] http://home.cern/sites/home.web.cern.ch/files/image/update-for_cern_people/2016/06/intlumirunall_image.png
- 1109 [36] website: <http://cds.cern.ch/journal/CERNBulletin/2014/24/News%20Articles/1706606>
- 1111 [37] website: <https://twiki.cern.ch/twiki/bin/view/CMSPublic/LumiPublicResults>